

Bulk mineralogy of lunar crater central peaks via thermal infrared spectra from the Diviner Lunar Radiometer: A study of the Moon's crustal composition at depth

Eugenie Song,¹ Joshua L. Bandfield,¹ Paul G. Lucey,² Benjamin T. Greenhagen,³ and David A. Paige⁴

Received 29 June 2012; revised 29 January 2013; accepted 25 February 2013; published 12 April 2013.

[1] The central peaks of lunar impact craters are thought to be composed of uplifted material originating from varying depths of the crustal column. The interpreted crystallization sequence of the early lunar magma ocean resulted in an anorthositic upper crust that may become progressively more mafic as it approaches the olivine-rich mantle. Emissivity spectra from the Lunar Reconnaissance Orbiter (LRO) Diviner Radiometer are used to derive the wavelength location of the Christiansen Feature (CF), which is sensitive to bulk silicate mineralogy. Here a survey of CF values has been performed for the central peaks of 135 complex craters, providing global and regional observations of the heterogeneity of crustal compositions. Crustal thickness models give context to the preimpact depth of the central peak material and its proximity to the crust-mantle boundary. This study has identified six craters with potentially ultramafic compositions within their central peaks. More common occurrences of mafic material, found in a wide variety of crater central peaks, show a silicate composition roughly similar to mare basalt or an olivine-bearing gabbro. The range of central peak CF values is similar to that of the rest of the lunar surface. Bulk mineralogy of the central peak material does not appear to be correlated with its crustal depth of origin, suggesting both lateral and vertical heterogeneity in crustal composition rather than a gradual transition from felsic to mafic composition. It is likely that the Moon's extensive cratering history has continually overturned the original crust, erasing any original systematic dependence of composition on depth or proximity to the mantle.

Citation: Song, E., J. L. Bandfield, P. G. Lucey, B. T. Greenhagen, and D. A. Paige (2013), Bulk mineralogy of lunar crater central peaks via thermal infrared spectra from the Diviner Lunar Radiometer: A study of the Moon's crustal composition at depth, *J. Geophys. Res. Planets*, 118, 689–707, doi:10.1002/jgre.20065.

1. Introduction and Background

1.1. Introduction

[2] The present-day lunar crust is a product of two highly energetic and interactive processes—the melting and subsequent crystallization of a diverse range of silicate lithologies over a wide range of scales and a persistent barrage of crater forming impacts that pulverize, overturn, and uplift the crust and its existing stratigraphy. Studies of terrestrial craters and Apollo samples along with remotely

sensed observations and sophisticated modeling of the Moon's formation and crustal evolution have provided a framework of how and when these processes occurred [Heiken *et al.*, 1991; Jolliff *et al.*, 2006].

[3] Based on the crystallization sequence of the young Moon's global magma ocean, cumulate layers are thought to have formed with large amounts of olivine at the crust-mantle interface and increasing proportions of orthopyroxene and clinopyroxene with decreasing depth [LAPST, 1985]. After about 75% of the magma ocean had crystallized, the aluminum content of the melt had increased enough to permit plagioclase saturation, and the high density of the residual magma allowed for lower-density plagioclase minerals to form a floating anorthositic crust [Warren, 1986; Shearer and Papike, 1999]. In the Apollo sample collection, diverse mafic coarse-crystalline rocks have been interpreted as plutons formed at shallow depths within the crust [Jolliff and Haskin, 1995]. The generally higher ratio of Mg to the sum of Mg and Fe of these rocks have led them to be referred to as the “Mg-suite” [Warner *et al.*, 1976]. Because the crust as a whole is more mafic than the known anorthosites, as much as 20% of the crust by volume could be composed of Mg-suite rocks or other mafic components [Taylor *et al.*, 1993].

¹Earth and Space Sciences, University of Washington, Seattle, Washington, USA.

²Hawaii Institute for Geophysics and Planetology, University of Hawaii at Manoa, Honolulu, Hawaii, USA.

³Jet Propulsion Laboratory, California Institute of Technology, Pasadena, California, USA.

⁴Department of Earth and Space Sciences, University of California at Los Angeles, Los Angeles, California, USA.

Corresponding author: E. Song, now at University of Hawaii at Manoa, Hawaii Institute of Geophysics and Planetology, 1680 East-West Road, POST 602, Honolulu HI 96822, USA. (eugesong@higp.hawaii.edu)

[4] Massive impacts during the Late Heavy Bombardment (~4.1–3.8 Ga) created numerous large basins. Basalt formed by the remelting of the mafic cumulates from earlier stages of magma ocean differentiation flooded most of the basins, creating the darker mare terrain (mainly 3.9–3.1 Ga) [BVSP, 1981]. Owing to the lack of atmosphere, few subsequent changes occurred that are not related to cratering or space weathering processes. Today's lunar regolith is a poorly consolidated layer generated from the constant meteoroid interactions with the bedrock [Hörz *et al.*, 1991].

[5] Using Earth-based telescopic near-IR spectroscopy, Pieters [1986] showed that the ejecta deposits of small craters that sample the upper kilometer of the lunar crust are relatively uniform in composition, probably because the surface has been exposed to intense mixing from impacts. To view the lunar crust below this mixed layer, Pieters studied the central peaks of large craters, which are composed of uplifted crustal material and expose rock originating from varying depths of the lunar subsurface. Since the studies of Pieters [1982, 1986], Tompkins and Pieters [1999], and Cahill *et al.* [2009] used visible and near-infrared (NIR) multispectral imaging obtained from lunar orbit to examine many more craters and distributed locally to demonstrate the compositional diversity of the lunar crust.

[6] Until recently, visible and NIR spectroscopy remained the only data available to study the composition of a large sample of central peaks. However, the Diviner Lunar Radiometer (Diviner) [Paige *et al.*, 2009] collected spectral data in the region of thermal emission near 8 μm that contains information complementary to that revealed by NIR data. Thermal multispectral imaging is especially sensitive to the ratio of feldspar to mafic minerals, which is crucial to understanding the basic lithology of lunar rocks [Greenhagen *et al.*, 2010].

[7] The focus of this study is to understand the distribution of deep seated crustal and potentially mantle-sourced material within the uplifted rock in crater central peaks using thermal infrared multispectral imaging. In this study, the mafic to feldspar proportions are determined for the central peaks of 135 craters with diameters ranging from 26 km to almost 200 km, providing a look at the range of felsic and mafic compositions originating from a variety of crustal depths around the globe.

1.2. Central Peaks: Drill Cores Into the Lunar Crust

[8] Understanding both the composition of the central peak as well as the depth the uplifted material originated from can be useful in mapping the vertical heterogeneity of the lunar crust, giving insight into the processes involved in lunar crust formation [e.g., Cahill *et al.*, 2009; Cintala and Grieve, 1998]. The uplifted peak's bulk composition should theoretically become more mafic as its depth of origin approaches the olivine-rich mantle.

[9] Crater morphology is strongly correlated with the diameter of the crater, with central peak formations typically occurring in craters with diameters between ~20 and 140 km [Melosh, 1989]. Terrestrial studies of complex craters have shown that the material making up the central peak is uplifted rock that originated below the floor of the crater [Grieve and Robertson, 1979; Grieve, 1981]. These impact events are intensely high energy, and the uplift of material can originate from depths of tens of kilometers in the crust [Wieczorek and Zuber, 2001]. The depth of origin of the uplifted central peak material is a function of crater diameter, where large craters are uplifting from a greater depth than small craters [Melosh, 1989; O'Keefe and Ahrens, 1993; Cintala and Grieve, 1998]. As in Cahill *et al.* [2009], this study assumes the minimum depth of origin coincides with the maximum depth of melting, which is $0.108^* \text{Crater Diameter}^{0.98}$ [Cintala and Grieve, 1998].

1.3. Spectral Features of Rock-Forming Silicates in the Lunar Environment

[10] Most lunar rocks are primarily composed of four minerals—plagioclase, pyroxene, olivine, and ilmenite [Lucey *et al.*, 2006]. Spectral features of silicate minerals occur in the midinfrared region of the spectrum between ~8 and 12 μm , where the asymmetric stretching mode of the Si–O tetrahedra results in a fundamental molecular vibration. The strength and wavelength location of the absorption feature is dependent upon the structure and cation makeup of the silicate crystal. Environmental factors such as ambient pressure and grain size also have significant influence on spectral shape [Estep-Barnes, 1977]. For powders in a vacuum, like on the Moon, these silicate optical properties are expressed as an emission peak known as the Christiansen Feature (CF) [Salisbury, 1993].

[11] The degree of silica polymerization is directly related to the composition of the magma and their formation temperatures (resulting in varying stages of fractional crystallization of a magma ocean). The strongest fundamental Si–O vibrational modes of these minerals form absorption features between 8 and 12 μm that shift toward shorter wavelengths as the lattice bond strength increases [Kahle *et al.*, 1993]. The CF occurs in the 7.5–9.0 μm wavelength range for silicates and is an emissivity maximum at wavelengths just shortward of the fundamental absorption features. The exact wavelength location of this maximum is correlated with the overall silica content (Table 1) within the measurement field of view and thus can be used as an indicator of bulk mineralogy.

[12] The CF emissivity peak has been shown to become more pronounced in a simulated lunar environment, as well as systematically shifted toward shorter wavelengths [Salisbury, 1993; Hapke, 1996; Henderson and Jakosky, 1994]. The CF peak occurs just prior to a fundamental molecular vibration band where the wavelength-dependent refractive index of

Table 1. Common Lunar Silicate Minerals—Their Molecular Structures [Estep-Barnes, 1977] and CF Positions [Greenhagen *et al.*, 2010].

Mineral	Silicate Class	Degree of Polymerization	Molecular Grouping	Si/O Ratio	CF Position
Olivine	Nesosilicate	Single tetrahedral	SiO_4^{4-}	Si/O = 0.25	8.67 μm (forsterite end-member)
Pyroxene	Inosilicate	Single chain	SiO_3^{2-}	Si/O = 0.33	8.25 μm (intermediate composition)
Plagioclase	Tectosilicate	Framework	SiO_2	Si/O = 0.50	7.84 μm (anorthite end-member)

the mineral rapidly changes (anomalous dispersion) and approaches the refractive index of the surrounding environment. This minimizes reflection at grain boundaries, and absorption is relatively low because of its proximity to the edge of the Reststrahlen feature (a fundamental vibration band that is undetectable in the lunar environment) [Lyon, 1965; Salisbury, 1997]. At the wavelength location of the CF, radiation can pass through the sample relatively freely [Mustard and Hays, 1997]. For daytime measurements, the material at several tens of microns depth is at a higher temperature than the immediate surface. As a result, radiance is higher at the more transparent wavelengths of the Christiansen peak [e.g., Henderson and Jakosky, 1994].

1.4. Compositional Studies of Lunar Crater Central Peaks

[13] Previous studies of central peak compositions have utilized data from telescopic instruments [Lucey et al., 1991; Pieters, 1982, 1986] and lunar orbiting near-infrared (NIR) multi- and hyperspectral instruments (e.g., Clementine UVVIS-NIR [Tompkins and Pieters, 1999; Cahill and Lucey, 2007; Cahill et al., 2009], Kaguya Spectral Profiler [Yamamoto et al., 2010; Matsunaga et al., 2008], Moon Mineralogy Mapper [Dhingra et al., 2011; Mustard et al., 2011]). The diagnostic mafic mineral absorption features seen in NIR spectroscopy has proven extremely useful for identifying a diverse range of mineralogies within central peaks [Cahill et al., 2009; Tompkins and Pieters, 1999].

[14] Tompkins and Pieters [1999] derived central peak compositions of 109 craters using Clementine UVVIS multispectral data (the study included five spectral bands ranging from 0.4 to 1.0 μm). Two spectral parameters were used for classification—"key ratio," a band ratio that estimates the relative abundance of mafic minerals, and "spectral curvature," the angle formed between the longer wavelength bands to distinguish between mafic minerals—particularly pyroxene compositions. Laboratory spectra of various mixtures of mineral end-members (olivine, orthopyroxene, clinopyroxene, anorthosite) were convolved with Clementine filters for comparison to the lunar data, allowing for estimation of the mineral abundances based on the two spectral parameters.

[15] Global trends in the Tompkins and Pieters [1999] study showed that the highlands crater peaks are consistent with gabbroic, noritic, or troctolitic anorthositic compositions (85%–90% plagioclase). Peaks of craters in or around basins are mostly composed of anorthositic norite and a wider range of gabbroic, noritic, or troctolitic anorthositic (80%–90% plagioclase). Basin craters also more frequently exhibited multiple lithologies. The six craters found with spectral signatures consistent with troctolitic compositions also contain anorthosite in their central peaks. The Tompkins and Pieters paper found differing proportions of mafic rock types between highlands and basin craters and also suggests a weak trend between crustal depth and composition (where more mafic-rich materials are associated with the deeper crust).

[16] The compositional analysis from Tompkins and Pieters [1999] was expanded to include comparisons to a dual-layer crustal thickness model by Wieczorek and Zuber [2001]. This model is based upon the assumption that the lunar crust is stratified into an anorthositic upper layer and noritic lower layer, where much of the crustal thickness

variation occurs within the upper layer. Based on central peak composition and depth of origin, the upper crust is composed of 88 ± 4 vol.% plagioclase and the most mafic lower crust contains 65 ± 8 vol.% plagioclase, which is more feldspathic than typical mare basalt with ~20–40 vol.% plagioclase [BVSP, 1981]. The study concludes that both the upper and lower crust could have formed by cumulate flotation in a magma ocean due to the high plagioclase content of both layers that would maintain buoyancy of the cumulate assemblage.

[17] Cahill et al. [2009] targeted 55 immature complex craters that are possibly excavating lower crust and/or mantle material in their central peaks using the approach of Wieczorek and Zuber [2001] and combined compositional modeling derived from Clementine UVVIS and NIR spectra (eight spectral bands between 0.75 and 2.0 μm) with depth of origin models to analyze crustal composition with depth. Clementine spectra were compared to modeled spectra based on radiative transfer theory, mineral optical constant data, and iron optical constant data in order to determine the proportions of olivine, orthopyroxene, clinopyroxene, and plagioclase in the peaks. The depth of origin of central peak material (a function of crater diameter) was combined with a single-layer crustal thickness model to compare each crater's central peak composition with its depth of origin relative to the crust-mantle interface. About half of the craters investigated are calculated to have plausibly uplifted material from within 5 km of the crust-mantle interface. The results of this work show a large diversity of lithologies in the regions included in Cahill's study (Procellarum KREEP Terrane, Feldspathic Highlands Terrane, and South Pole-Aitken basin), with the majority of peaks consisting of mafic composition similar to Mg-suite rocks.

[18] Cahill et al. [2009] found that peaks with mafic lithologies were generally located in the South Pole–Aitken (SPA) and Procellarum KREEP Terranes within 50 km of the crust-mantle boundary. This is consistent with a crust with increasingly mafic mineralogy as it approaches the mantle, although these mafic peaks are also confined to regions with relatively low crustal thicknesses. Anorthositic peaks were largely confined to the highlands but also appeared throughout the crustal column, which is inconsistent with a simple increasingly mafic crust with depth [Ryder and Wood, 1977] and suggests a more complex formation mechanism.

[19] Olivine-rich exposures have been located in concentric regions around SPA, Imbrium, and Moscovense impact basins where the crust is relatively thin [Yamamoto et al., 2010]. The olivine-rich lithologies, identified using NIR hyperspectral data from the Spectral Profiler onboard the JAXA Kaguya orbiter, were often detected within small, fresh craters in and around these impact basins where the olivine-rich layers were initially covered by ejecta or heavily space weathered prior to excavation by later impacts Yamamoto et al. [2010] propose that the observed olivine can be attributed to Mg-rich plutons or excavation of the mantle during the basin forming impacts.

[20] In Cahill et al. [2009], Copernicus crater was found to contain the highest olivine abundance with 72 vol.% olivine (troctolite) and may be an example of material uplifted from the mantle or near the crust-mantle interface. Several studies identified olivine in NIR spectra of Copernicus crater's central peak as well as three small areas in the northern crater walls

[Pieters, 1982; Lucey *et al.*, 1991; Le Mouélic and Langevin, 2001; Pinet *et al.*, 1993]. The inner walls of complex craters are terraced due to rim collapse near the end of crater formation, so the walls of the terraces may expose crustal stratigraphy down to the depth of the crater but they are not uplifted in the same manner as central peaks [Melosh, 1989].

2. Data and Methods

2.1. Diviner Instrument and Data Acquisition

[21] Diviner data are sensitive to bulk silicate mineralogy that can help clarify ambiguities in mineral abundances determined by NIR data [Lucey and Greenhagen, 2012]. Near-infrared spectroscopy can enhance the interpretation of the CF data, allowing bulk composition to be parsed into the individual minerals present in the mixture. Greenhagen *et al.* [2010] showed an analysis of the global distribution of CF values from Diviner data and identified exposures of a range of lithologies, including ultra-silica-rich soils [Glotch *et al.*, 2010]. In this study, we focus on cataloguing lithologies specifically within complex craters at ~ 0.25 km resolution in order to better understand the composition and distribution of mafic minerals throughout the crustal column.

[22] Diviner is a multispectral pushbroom radiometer launched in 2009 onboard the Lunar Reconnaissance Orbiter (LRO). Diviner has nine spectral channels: channels 1 and 2 measure broadband reflected solar radiation between 0.35 and 2.8 μm , and channels 3–9 measure emitted thermal radiation from 7.5 to 400 μm [Paige *et al.*, 2009]. Diviner's three shortest thermal infrared channels (3–5) have narrow passbands centered around the 8 μm region (7.55–8.05 μm , 8.10–8.40 μm , and 8.38–8.68 μm) where the CF occurs for most lunar compositions [Paige *et al.*, 2009]. Each of the nine channels is composed of 21 element linear arrays of 240 by 480 μm pixels with a ground resolution of ~ 160 m (cross track) by 320 m (along track) from the typical 50 km polar mapping orbit of the LRO primary mission [Paige *et al.*, 2009].

[23] The Diviner Reduced Data Records (RDR) include the latitude and longitude location at the center of each detector's instantaneous field of view (FOV). The effective FOV is broadened due to spacecraft movement during the 128 ms sample integration time. The broadening occurs in the along-track direction that can be rotated slightly relative to north depending on spacecraft orientation. The rectangular shape of the Diviner pixels and along-track smear precludes the use of a simple camera model more typically used in the production of imaging data sets. In order to describe the full spatial extent of the broadened data point, a two-dimensional Monte Carlo routine generates additional data points with identical data fields as the original point with the exception of their latitude and longitude locations, which are randomly produced and weighted by the calculated distribution of source radiance within each Diviner FOV. The binned results from this technique show significant improvements in image quality—the spectral channels are more accurately aligned with each other, eliminating the fringing artifacts found on topographic boundaries in derived products like CF value maps.

[24] The Diviner Level 1b radiance data used in this study were collected from 28 August 2009 through 26 September 2011 (available via Planetary Data System, <http://pds.nasa.gov/>).

Data were restricted to local times between 1,000 and 1,400 to avoid severe illumination conditions that can cause the CF position to shift [Greenhagen *et al.*, 2010]. Two quality flags from the Diviner RDR were utilized—activity flag = 110 (standard nadir observations) and quality flag for calibration = 0 (best quality data, the calibration marker occurs within nominal time difference from a calibration point). A full description of the standard Diviner data processing method, including FOV correction, is available in the Diviner RDR and derived products Software Interface Specification (SIS) version 1.11.

2.2. Data Processing

[25] For each Level 1B data point, the Diviner measurement's footprint is projected by locating the FOV onto a 2 km resolution digital elevation model (DEM) based on data from the Lunar Orbiter Laser Altimeter (LOLA) onboard LRO [Zuber *et al.*, 2010]. As described in section 2.1, 2,000 points per measurement that define the boundary of the effective FOV are added to the data stream to be further processed with the rest of the data. The data are projected a final time onto the LOLA DEM to provide target latitude and longitude for every point that is then ready to be binned. These processing steps are essential for eliminating artifacts in the final CF maps caused by between-band misregistration coupled with small-scale or abrupt topographic variations (which can shift the CF value by several tenths of a micron along and around sharp topographic boundaries).

[26] Following topographic and FOV corrections, calibrated radiance data from channels 3 to 5 were binned at 128 pixels per degree (~ 230 m per pixel at the equator) and brightness temperatures were calculated for each band based on a look-up table constructed from Planck radiance convolved with the Diviner filter response functions. As shown in Greenhagen *et al.* [2010], we assume the peak of a parabola fit to the 3-point brightness temperature spectrum is the surface kinetic temperature. CF values were determined by calculating the wavelength at the maximum of the parabola (Figure 1) [Glotch *et al.*, 2010; Greenhagen *et al.*, 2010, see supporting online material].

[27] The random error associated with the Diviner CF value was approximated using data from a relatively flat, featureless surface at local times ranging between 1,000 and 1,400. The sampled region is in the nearside mare centered around -54° E, 0.26° N where there are no craters greater than 1 km in diameter. The data were processed in the same manner as described above. A uniform region containing $\sim 1,100$ to 1,600 pixels within a single orbit track was selected for each local time. Although the sampled regions for each local time do not directly overlap due to limitations in coverage, Clementine-derived FeO and maturity maps show compositional uniformity within the sampled regions such that the only variations in CF value are due to local time and random error. The mean and standard deviation CF values are plotted versus local time in Figure 2. Data collected at noon local time have the lowest CF value standard deviation (0.010 μm), and as local time strays from noon, the CF value standard deviation steadily increases (up to 0.017 μm). This systematic uncertainty is an order of magnitude smaller than the CF value variations due to anisothermality and other effects described above, so it is considered negligible for the purposes of this study.

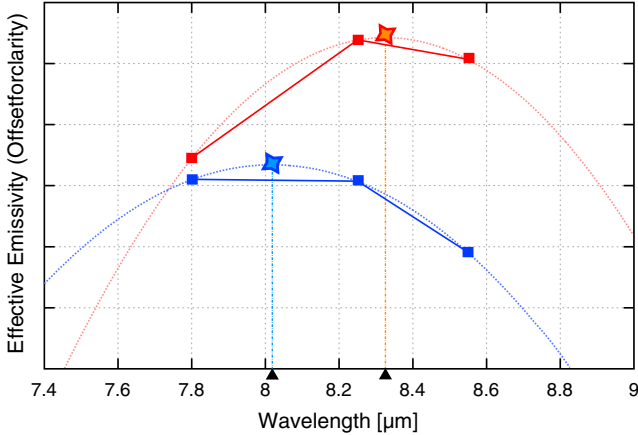


Figure 1. Use of a parabolic fit to 3-point Diviner (7.80, 8.25, and 8.55 μm) emissivity spectra to locate Christiansen Feature emissivity maximum. The red trace is an example of a predominantly mafic composition, uplifted in the central peak of Barringer crater where the CF value—the interpolated emissivity maximum—occurs at 8.36 μm . The blue trace is from a more felsic region near the south wall of the same crater, with a CF value of 8.02 μm .

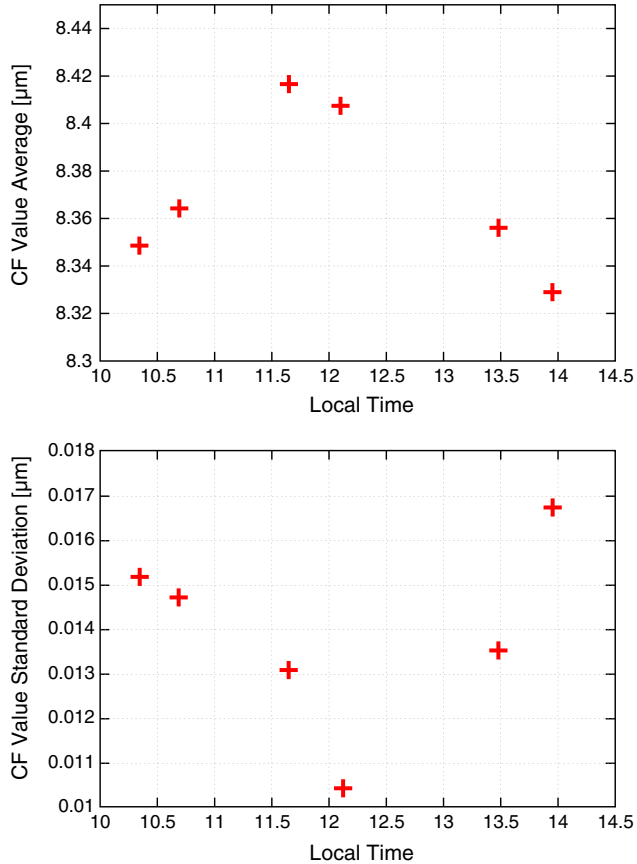


Figure 2. Random error in Diviner CF value. (top) Average CF value versus local time. (bottom) Standard deviation of CF value versus local time.

2.3. Anomalous CF Shifts

[28] Several properties other than bulk composition shift the wavelength location of the CF in the lunar environment, including anisothermality and space weathering [Bandfield *et al.*, 2011b; Greenhagen *et al.*, 2010; Lucey *et al.*, 2010]. We also find an additional property influencing CF that is likely related to temporal variations in thermal gradients. Although the controlling processes for some of these effects are not yet fully characterized, we have investigated and described these processes and quantified the magnitude of their effect on the CF. Data that were clearly dominated by these effects were discarded or masked out.

2.3.1. Anisothermality

[29] The FOV of a single observation always contains a range of temperatures—a phenomenon called anisothermality. The rough lunar surface contains a distribution of solar incidence angles within the measurement FOV due to surface topography primarily at millimeter scales [e.g., Shepard *et al.*, 1995]. The brightness temperature measured in each footprint is the weighted average of the radiance for the temperatures present. The resultant radiance spectrum, a combination of Planck radiance curves for the mixture of temperatures within the FOV, is skewed heavily toward the warmer temperature present such that the measured brightness temperature will lie somewhere between the average temperature and the highest temperature. The magnitude of skew in the spectrum toward the warmer brightness temperatures in the FOV is highly nonlinear and increases with decreasing wavelength [Bandfield, 2009; Colwell and Jakosky, 2002; Smith, 1967; Spencer, 1990].

[30] If emissivity is derived assuming a single temperature, anisothermality introduces a negative slope to the effective emissivity spectrum that becomes steeper with an increasing range of temperatures present. This translates to a shorter wavelength CF position for more anisothermal surfaces [Bandfield *et al.*, 2011b; Greenhagen *et al.*, 2010]. The degree of anisothermality due to surface roughness is dependent upon solar incidence angle, as morning and evening Sun angles create Sunlit and shaded slopes with greatly differing temperatures [Bandfield *et al.*, 2011a]. The effect becomes negligible at local noon as slopes at all azimuths approach the same temperature. The magnitude of shifts to the CF position due to anisothermality can be up to 0.4 μm at high solar incidence angles but is typically $<0.1 \mu\text{m}$ with observations close to noon and is easily avoided by using observations with low angles of solar incidence.

[31] Large-scale temperature boundaries, such as between the wall and floor of a crater, also create significant shifts in the CF. The binned CF value image for each crater was masked due to anisothermality effects in regions with sharp temperature transitions. The mask was created by taking the derivative of channel 4 radiance with respect to lateral distance and discarding data with values greater or less than 2 standard deviations from its mean, which was found to be the optimal threshold for this data set. Regions where radiance values are transitioning between extremes—such as the interface between a central peak and the crater floor—were discarded by the mask (Figure 3). The range of temperatures within a single pixel is much greater in these topographic interfaces, so when a single surface temperature is assumed, there is a significant shift in the

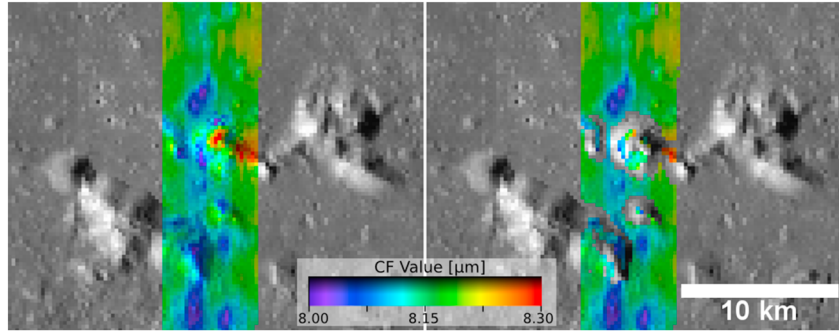


Figure 3. An example of the data mask used to discard Diviner CF data that is likely to be dominated by the effects of anisothermality, particularly on topographic boundaries where severe temperature changes occur at scales smaller than Diviner’s footprint. Close-up of the central peaks of Copernicus, with colorized CF value from two Diviner orbits stretched from 8.0 to 8.3 μm over WAC mosaic background. Left and right image are unmasked and masked CF value maps, respectively.

CF value, greatly affecting mineralogical interpretation [Bandfield *et al.*, 2011a].

2.3.2. Space Weathering

[32] The surface of the Moon is constantly bombarded by micrometeorites, solar wind, and cosmic rays. These processes alter the optical properties of the soil by coating nanophase iron on grain surfaces as well as forming agglutinates (glassy aggregates) [e.g., Noble *et al.*, 2001; Taylor *et al.*, 2001]. Both of these forms of weathering cause a darkening of the soil at visible wavelengths, and nanophase iron implantation produces a red spectral slope into the NIR [Le Mouélic *et al.*, 2000].

[33] An estimate for the degree of maturity of lunar soils can be derived from Clementine UVVIS maps using the optical maturity parameter (OMAT) algorithm developed by Lucey *et al.* [2000]. These maps show that central peaks and crater walls are generally less weathered than surrounding surfaces. Mass wasting is common on the relatively steep slopes of central peaks and crater walls, exposing fresh, unweathered material.

[34] The alteration of optical properties has shown to shift the CF position as well [Glotch *et al.*, 2012; Lucey *et al.*, 2010]. The magnitude of this shift can be determined by analyzing the CF positions associated with the Reiner Gamma albedo feature in the Procellarum basin. The Reiner Gamma feature shows variations in OMAT values without other effects (e.g., compositional or topographic variations), allowing for the isolation of the space weathering effect on CF position. An increase of 0.15 in the maturity parameter calculated using Clementine data (the value increases with less weathered, younger soils; ~4% change in albedo) corresponds with a decrease in CF value of 0.08 μm . This range of OMAT values is typical of those observed over surfaces of a variety of maturities within the complex craters studied here (~0.20–0.35). The OMAT constraint invoked in Cahill *et al.* [2009], where immature craters ($\text{OMAT} > 0.3$) were examined, is not applied in this study because the relationship between the CF value and OMAT parameter is not yet fully understood.

2.3.3. Additional Effects on the CF Position

[35] An additional effect on spectral emissivity has been found in this study that also appears to be largely dependent upon topography, solar insolation, and local time. The physical processes responsible for these effects have not

been fully characterized, but their influence on the CF position can be quantified with inspection of the data at various slopes and local times. The apparent dependence of this effect on surface temperature shifts the CF position in the opposite direction of the CF position shift due to lateral anisothermality (as discussed in section 2.3.1—where CF generally decreases with increasing solar incidence angle).

[36] The magnitude of this effect is asymmetrical about local noon, which suggests that this effect is dependent upon the subsurface thermal gradient that varies in intensity throughout the day. It has been shown previously that thermal gradients within the regolith of bodies in vacuum environments have an effect on mid-IR spectral features [Cooper *et al.*, 2002; Henderson and Jakosky, 1994, 1997; Salisbury *et al.*, 1973], but there are additional factors such as infrared and reflected solar heating from nearby surfaces that have not yet been quantified. Slopes opposite that of a topographic high (e.g., a central peak) experience differing amounts of integrated solar insolation throughout the lunar day and it is important to note both the solar incidence angle on a surface at the time of observation as well as the elapsed time that surface has been heated in order to fully characterize near-surface thermal gradients and their effects on the CF wavelength.

[37] The effect on CF position is most prominent prior to noon local time, where pixels showing low temperature (usually on shaded slopes) are associated with relatively high CF values and pixels showing high temperature (Sunlit slopes) are associated with relatively low CF positions (Figure 4, 11 A.M.). With local times after noon (Figure 4, 1 P.M.), the effect is apparent for the lower temperature pixels up to ~383 K, while the higher temperature pixels (>385 K) behaved as expected based on CF position shifts due to anisothermality alone with a higher CF position correlated with higher surface temperature.

[38] This effect consistently causes shifts in CF position on opposite sides of a topographic slope as well as opposing crater walls. This is seen most prominently within single orbit tracks with fixed local time on north and south facing slopes. Observing the effect between east and west facing slopes is more difficult simply because it typically requires two separate orbit tracks acquired near the same local time to provide data coverage on laterally opposing slopes. The CF value can vary by ~0.2 μm due to this effect with data

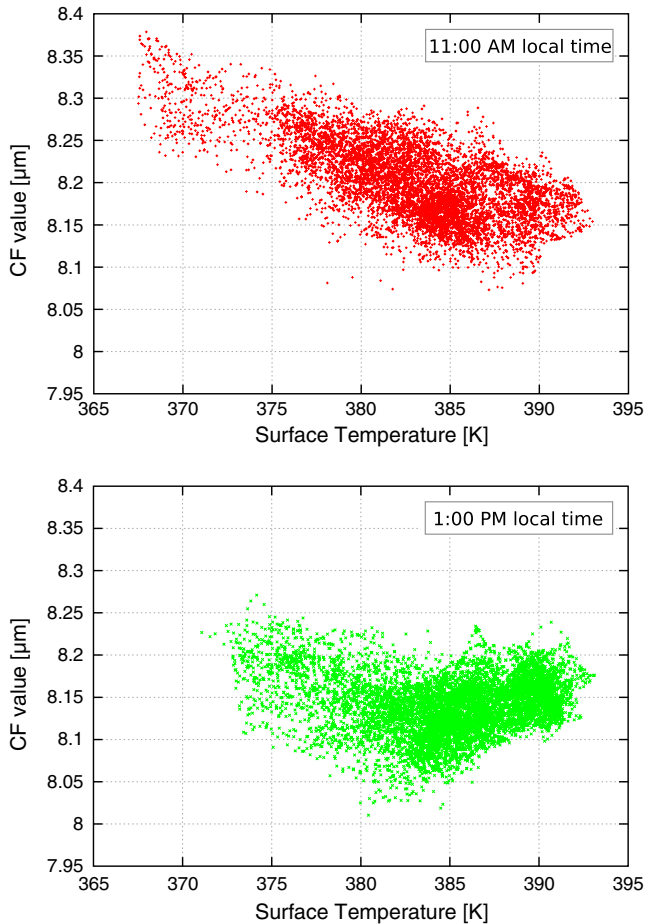


Figure 4. Scatter plot of CF value versus surface temperature. Diviner data collected before (red) and after (green) local noon over the same location in the highlands with negligible compositional variation. The dominant effect for the prenoon data (red) is a shift of CF values to shorter wavelengths with increasing temperature. A shift in CF value to longer wavelengths with higher temperatures is due to anisothermality; the 1:00 P.M. CF value variation is almost entirely due to anisothermality above 385 K due to variable solar incidence on local slopes as described in section 2.3.1.

collected prior to local noon. In order to avoid sampling CF data where this effect occurs, central peak sample regions were limited to areas of relatively constant temperature (<10 K variation) that do not extend beyond a single topographic facet at Diviner's spatial resolution.

2.4. Crater Selection and Processing

[39] A list of complex craters within 30° latitude of the equator was compiled based on the Gazetteer of Planetary Nomenclature maintained by the USGS Astrogeology Science Center [IAU WGPSN, <http://planetarynames.wr.usgs.gov>]. Diviner CF data are prone to the harsh solar angles at higher latitudes, so craters beyond 30° were not included. Twenty-two complex craters that were not listed in the Catalog were also identified using the Lunar Reconnaissance Orbiter Camera Wide Angle Camera (LROC WAC) Equatorial Mosaic and included in this study [Robinson *et al.*, 2010]. Criteria used to pick the craters for this analysis are (a) easily identifiable and unambiguous central peaks resolvable at Diviner spatial resolution, (b) Diviner data coverage over the one or more of the crater central peaks, and (c) Diviner data acquired within 2 h of noon local time to minimize CF value shifts that are a function of solar incidence angle.

[40] From the 268 craters initially examined, craters with data that were clearly dominated by noncompositional shifts to the CF position within their central peaks (identified by the distinctive CF shifts over topographic boundaries) were discarded from the survey. For the remaining 135 craters (Figure 5), data from the central peaks were isolated from the rest of the image with a polygon mask that was drawn for each crater. Regions with highly variable topography (e.g., the crest or base of the peak) were avoided, so the masks generally represent the CF values from one relatively uniform side of the central peak. Because topographic features degrade over time due to impact cratering and regolith formation, the oldest craters in this survey often had a larger area that we were able to sample from the central peak (e.g., Alpetragois crater, Figure 6) than newer craters with sharp topographic features (e.g., Copernicus crater, Figure 3), though this did not affect the final results.

[41] Data within the polygon mask were averaged to determine the mean CF value of each crater's central peak.

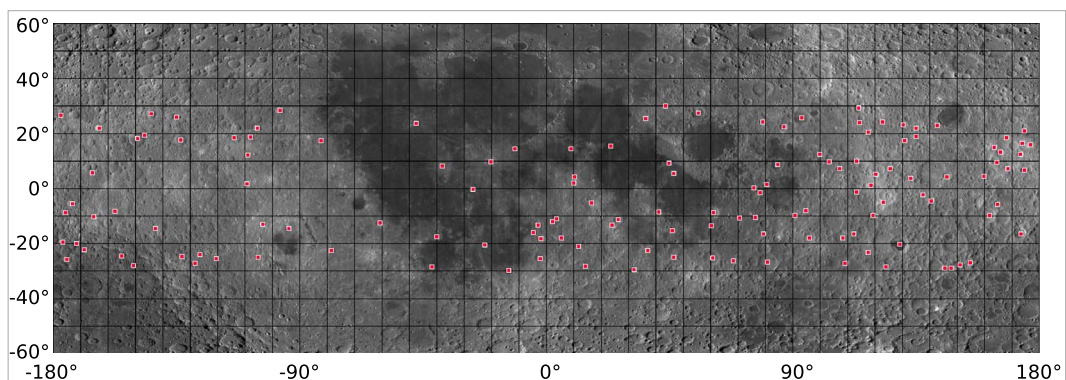


Figure 5. Location of the 135 craters examined in this study on a LROC WAC basemap from -60° to 60° latitude. Gridlines every 10° .

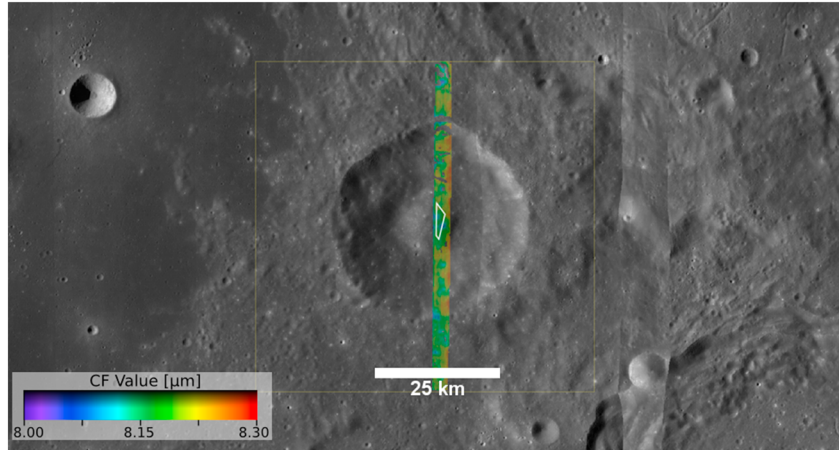


Figure 6. An example of a degraded crater (Alpetragius) with smoothed topographic boundaries. Overlain on the LROC WAC basemap is the colorized CF value image (stretched from 8.0 to 8.3 μm) with a white polygon around the region sampled for average CF value for this crater's central peak.

If multiple lithologies are present in the sampled region, the measured CF value is a linear mixture of each lithology's CF value (proportional to their abundance). Local crustal thickness [Wieczorek *et al.*, 2006] and Clementine-derived FeO abundance [Lawrence *et al.*, 2002], degree of maturity (OMAT) [Lucey *et al.*, 2000], and 750 nm reflectance were also determined for the same region. Clementine-derived maps for each crater were shifted manually to ensure they aligned with the LRO WAC global mosaic and Diviner CF maps. Inner crater walls were also examined for any signs of mafic exposures; however, the highly variable terraced crater walls are often extensively masked and only one acceptable compositionally anomalous surface (a olivine-rich feature in the inner wall of Copernicus crater) was identified in this category.

[42] Osinski *et al.* [2011] showed examples of impact melt draped over central peaks in a thin melt veneer. The melt veneer can cover significant portions of the central peak structures, making it appear darker than the rest of the peaks. Identifying impact melt on the 135 craters surveyed here was not possible due to the limited coverage of high-resolution imagery, so the effect of this melt to the CF value has not yet been quantified.

2.5. Supporting Data

[43] The CF value data for each crater were compared against NIR hyperspectral imagery from the Moon Mineralogy Mapper to ensure that shifts in CF value are correlated with compositionally distinct features rather than temperature-dependent and space-weathering anomalies. Crustal thickness maps [Wieczorek *et al.*, 2006] allowed for a correlation of central peak CF values and inferred composition at various depths with proximity to the mantle.

[44] The average central peak CF values were compared with iron abundance and optical maturity (OMAT) data from the sampled region. These maps were derived from Clementine spectral reflectance data [Lawrence *et al.*, 2002; Lucey *et al.*, 2000], and the LROC WAC global mosaic and LOLA topography provided spatial context for the measurements.

[45] Central peaks with CF positions indicative of ultramafic compositions were further explored using hyperspectral

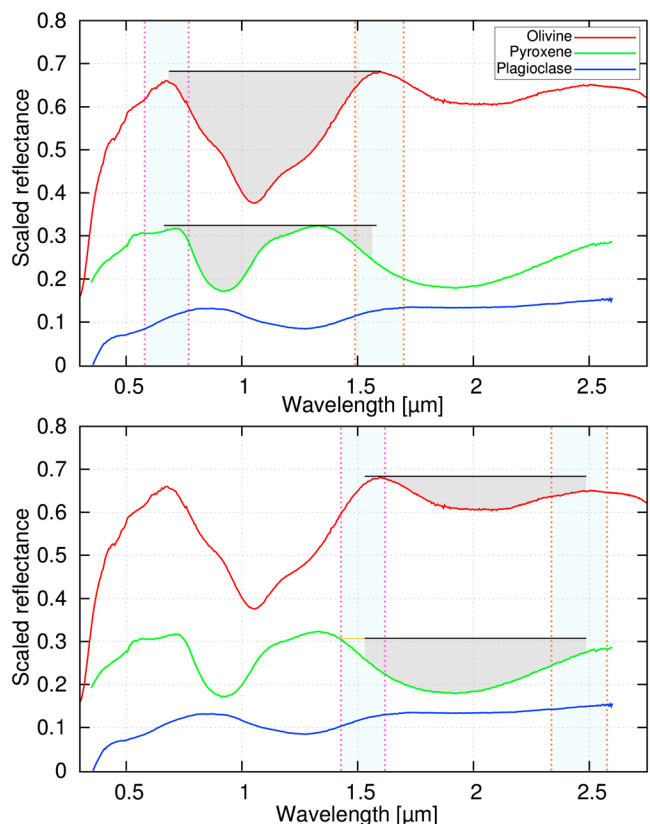


Figure 7. Creating olivine index maps from M^3 hyperspectral data. NIR laboratory spectra of olivine, pyroxene, and plagioclase separates from lunar samples [Bishop *et al.*, 1995; Mustard and Pieters, 1989] show the characteristic broad 1 μm absorption feature of olivine, 1 and 2 μm absorption features of pyroxene, and relatively featureless plagioclase spectra. (top) Integrated band depth of the 1 μm absorption feature. (bottom) Integrated band depth of the 2 μm absorption feature.

NIR imagery from the Moon Mineralogy Mapper (M^3) onboard Chandrayaan-1 spacecraft [Pieters *et al.*, 2009].

Table 2. Central Peak Compositional Results for 135 Craters, Sorted by Descending CF Value (Most Mafic to Most Felsic)^a

Crater Name	Lat. [°]	Lon. [°]	Diameter [km]	Avg CF Value [μm]	σ CF [μm]	Avg OMAT	Avg FeO [wt.%]	Crust (T) [km]	Peak Depth of Origin (D) [km]	Prox. to C-M Boundary (T - D) [km]	Peak Origin Normalized to Crustal Thickness ((T - D) / T * 100) [%]
1 Eratosthenes	14.47	348.65	58.77	8.48	0.04	0.19	15.21	38.5	8.9	29.6	76.9
2 Plummer	-24.73	205.13	67.52	8.42	0.03	0.18	10.27	36.1	10.3	25.8	71.5
3 Scaliger	-27.28	109.10	86.40	8.39	0.08	0.22	10.38	43.3	13.5	29.9	68.9
4 Taruntius	5.48	46.54	57.32	8.39	0.02	0.21	13.51	46.0	8.6	37.4	81.2
5 Barringer	-28.20	209.46	66.89	8.36	0.03	0.22	15.20	26.8	10.2	16.6	61.9
6 Gutenberg	-8.67	41.17	69.45	8.31	0.02	0.18	8.71	56.0	10.6	45.3	81.0
7 Plinius	15.34	23.65	42.94	8.30	0.05	0.20	10.60	43.3	6.3	37.0	85.4
8 Balzac	-8.23	94.95	34.80	8.29	0.04	0.20	5.06	54.7	5.0	49.7	90.8
9 Icarus	-5.58	187.00	93.73	8.27	0.03	0.23	4.95	63.5	14.7	48.9	76.9
10 Stratton	-5.76	164.89	69.76	8.26	0.01	0.20	4.93	39.0	10.7	28.3	72.6
11 Buisson	-1.36	113.26	62.13	8.26	0.02	0.20	7.51	61.6	9.4	52.2	84.7
12 da_Vinci	9.06	44.93	37.46	8.26	0.02	0.19	10.92	54.1	5.5	48.6	89.9
13 Albategnius	-11.20	3.96	130.84	8.26	0.03	0.19	7.01	56.4	21.1	35.3	62.6
14 Agrrippa	4.08	10.47	43.75	8.25	0.03	0.24	7.57	56.4	6.5	49.9	88.6
15 Doppelmayr	-28.52	318.47	65.08	8.24	0.02	0.18	15.21	30.4	9.9	20.5	67.4
16 Sierpinski	-27.22	154.97	69.08	8.23	0.05	0.20	6.89	38.6	10.6	28.1	72.7
17 Al_Khwarizmi	7.09	107.12	58.55	8.22	0.03	0.22	6.18	40.4	8.8	31.5	78.1
18 Purbach	-25.57	357.97	119.27	8.22	0.03	0.21	9.01	48.3	19.1	29.2	60.5
19 Klein	-12.01	2.48	43.47	8.21	0.03	0.21	7.27	52.3	6.4	45.9	87.8
20 Hilbert	-18.00	108.43	162.55	8.21	0.03	0.20	5.68	53.7	26.6	27.1	50.4
21 Gavrilov	17.37	130.97	61.62	8.21	0.02	0.21	5.37	47.3	9.3	37.9	80.2
22 Lohse	-13.74	60.28	43.34	8.21	0.05	0.22	8.37	53.1	6.4	46.7	88.0
23 Kapteyn	-10.80	70.51	49.51	8.21	0.02	0.22	7.15	41.9	7.4	34.5	82.4
24 Pannekoek	-4.63	140.67	67.50	8.21	0.02	0.22	4.86	64.2	10.3	53.9	84.0
25 Behaim	-16.59	79.41	56.21	8.20	0.02	0.20	7.13	49.6	8.5	41.1	82.9
26 crater_05	-28.56	124.19	38.87	8.20	0.02	0.21	5.69	44.4	5.7	38.7	87.2
27 Orlov	-25.78	185.22	63.75	8.20	0.04	0.25	11.95	18.3	9.7	8.6	46.9
28 Cyrillus	-13.29	24.07	98.09	8.19	0.04	0.24	5.29	61.1	15.4	45.7	74.8
29 Butlerov	12.04	251.16	38.77	8.19	0.02	0.25	6.43	47.9	5.7	42.3	88.2
30 De_Vries	-19.67	183.57	60.30	8.19	0.05	0.21	8.49	40.7	9.1	31.5	77.6
31 Lansberg	-0.31	333.34	39.79	8.18	0.03	0.24	14.20	44.3	5.8	38.4	86.8
32 Hubble	22.26	86.91	79.58	8.17	0.05	0.23	5.37	48.5	12.3	36.2	74.6
33 Neper	8.70	84.60	144.32	8.17	0.05	0.17	6.39	37.1	23.4	13.7	36.8
34 crater_39	-8.84	184.56	88.13	8.17	0.02	0.22	4.30	48.1	13.7	34.3	71.4
35 Glazenap	-2.32	137.71	38.96	8.17	0.03	0.22	5.19	71.4	5.7	65.7	92.0
36 Brunner	-9.83	90.88	52.65	8.17	0.03	0.21	5.00	47.6	7.9	39.7	83.4
37 crater_01	-29.03	147.89	73.53	8.17	0.06	0.22	6.44	48.5	11.3	37.2	76.7
38 Alpetragius	-16.05	355.45	40.02	8.16	0.03	0.21	8.59	50.2	5.9	44.4	88.3
39 crater_13	7.22	125.50	41.08	8.16	0.01	0.23	5.93	57.4	6.0	51.4	89.5
40 Siedentopf	21.97	135.14	62.70	8.15	0.03	0.21	4.67	54.1	9.5	44.6	82.4
41 Joliot	25.65	93.39	169.25	8.15	0.03	0.19	6.95	41.8	27.8	14.0	33.5
42 La_Perouse	-10.64	76.24	80.40	8.15	0.03	0.24	6.16	46.1	12.4	33.6	73.0
43 crater_17	18.91	135.09	34.44	8.15	0.03	0.23	4.80	48.9	5.0	43.9	89.8
44 Von_der_Pahlen	-24.88	227.11	53.89	8.15	0.03	0.24	6.38	98.7	8.1	90.6	91.8
45 Back	1.31	80.63	34.63	8.15	0.02	0.21	7.38	33.0	5.0	28.0	84.8
46 Sirsalis	-12.51	299.49	40.20	8.15	0.03	0.26	8.60	48.5	5.9	42.6	87.9
47 Laue	28.37	262.92	89.17	8.15	0.04	0.18	7.09	41.3	13.9	27.4	66.3
48 Copernicus	9.62	339.92	96.07	8.14	0.02	0.31	6.73	39.5	15.1	24.5	61.8
49 Leuschner	1.60	250.88	50.14	8.14	0.02	0.24	5.14	48.6	7.5	41.1	84.6
50 Keeler	-9.86	161.96	158.07	8.14	0.02	0.22	4.36	41.9	25.8	16.1	38.3
51 Pitatus	-29.91	346.44	100.63	8.14	0.03	0.21	8.60	42.8	15.9	26.9	62.9
52 Nobili	0.14	75.86	41.79	8.14	0.01	0.19	7.72	56.3	6.1	50.2	89.1
53 Vernadskiy	23.05	130.25	91.97	8.14	0.02	0.21	5.55	52.6	14.4	38.2	72.6
54 crater_19	23.83	114.25	34.59	8.14	0.02	0.23	7.29	40.7	5.0	35.7	87.7
55 Pontanus	-28.48	14.34	55.66	8.13	0.04	0.22	5.48	59.0	8.4	50.6	85.8
56 Papaleksi	9.42	164.58	97.67	8.13	0.03	0.23	4.10	37.9	15.4	22.5	59.5
57 crater_09	-14.64	217.25	43.44	8.13	0.04	0.22	6.31	72.2	6.4	65.8	91.1
58 Maunder	-14.54	266.16	53.80	8.13	0.05	0.27	7.95	29.5	8.1	21.4	72.6
59 Borda	-25.24	46.51	47.40	8.13	0.02	0.23	5.66	55.5	7.0	48.4	87.3
60 Meggers	24.19	122.82	51.16	8.12	0.04	0.22	5.67	44.5	7.6	36.9	82.8
61 Colombo	-15.28	46.11	79.02	8.12	0.07	0.20	6.25	52.9	12.2	40.7	76.9
62 Green	3.68	133.15	68.28	8.11	0.03	0.20	5.75	63.2	10.4	52.7	83.5
63 Arzachel	-18.27	358.01	96.99	8.11	0.04	0.25	7.98	54.8	15.2	39.5	72.2
64 crater_06	-26.38	68.47	35.99	8.11	0.05	0.26	9.76	48.9	5.2	43.7	89.3
65 Belyaev	22.99	142.98	53.56	8.10	0.03	0.22	4.29	55.5	8.0	47.5	85.5
66 Abenezra	-21.01	11.88	43.19	8.09	0.03	0.24	5.69	55.3	6.4	49.0	88.5
67 crater_02	-24.19	233.61	51.17	8.09	0.03	0.26	5.52	98.8	7.6	91.1	92.3
68 Airy	-18.16	5.58	38.90	8.09	0.02	0.26	6.34	49.1	5.7	43.4	88.4
69 Moiseev	9.52	103.31	61.22	8.09	0.02	0.27	6.18	48.1	9.3	38.9	80.7

Table 2. (continued)

Crater Name	Lat. [°]	Lon. [°]	Diameter [km]	Avg CF Value [μm]	σ CF [μm]	Avg OMAT	Avg FeO [wt.%]	Crust (T) [km]	Peak Depth of Origin (D) [km]	Prox. to C-M Boundary (T - D) [km]	Peak Origin Normalized to Crustal Thickness ((T - D) / T * 100) [%]
70 Necho	-5.23	123.24	33.78	8.09	0.01	0.35	6.60	54.6	4.9	49.7	91.1
71 crater_33	12.44	99.97	44.09	8.09	0.02	0.00	0.00	54.8	6.5	48.3	88.1
72 Ctesibius	1.02	118.56	32.10	8.08	0.02	0.31	6.18	51.7	4.6	47.1	91.1
73 Cleomedes	27.46	55.51	130.77	8.08	0.06	0.25	4.30	50.3	21.1	29.2	58.1
74 Tsolkovskiy	-20.46	129.06	184.39	8.08	0.04	0.25	5.12	45.3	30.5	14.7	32.6
75 crater_12	5.64	194.30	48.30	8.08	0.02	0.24	5.24	58.3	7.2	51.1	87.7
76 Van_Vleck	-1.71	78.15	33.48	8.08	0.03	0.20	6.17	38.8	4.8	34.0	87.5
77 Godin	1.80	10.14	33.55	8.08	0.05	0.28	7.29	61.1	4.8	56.2	92.1
78 Humboldt	-26.85	80.76	199.46	8.07	0.03	0.22	3.91	35.3	33.2	2.1	5.8
79 Theophilus	-11.48	26.25	98.59	8.07	0.06	0.28	4.32	33.9	15.5	18.4	54.2
80 crater_23	-29.22	145.73	42.73	8.07	0.02	0.27	8.62	40.0	6.3	33.7	84.3
81 Romer	25.38	36.42	40.82	8.07	0.04	0.31	10.40	53.6	6.0	47.6	88.8
82 Schuster	4.20	146.41	103.49	8.07	0.02	0.22	3.51	51.5	16.3	35.2	68.3
83 Langrenus	-8.86	61.00	131.98	8.06	0.03	0.00	0.00	45.5	21.3	24.2	53.3
84 Spencer_Jones	13.06	165.96	88.19	8.06	0.03	0.26	3.96	51.4	13.8	37.7	73.3
85 Valier	6.67	174.53	65.06	8.06	0.02	0.24	3.78	51.6	9.9	41.7	80.8
86 crater_10	-8.48	202.63	54.56	8.06	0.02	0.22	4.02	51.2	8.2	43.0	84.0
87 crater_08	-22.59	37.23	26.66	8.06	0.02	0.21	5.53	50.1	3.8	46.3	92.5
88 Skłodowska	-18.09	96.15	125.55	8.06	0.04	0.26	6.16	43.6	20.1	23.5	53.8
89 Taylor	-5.37	16.63	39.09	8.05	0.02	0.22	6.38	60.6	5.7	54.9	90.6
90 Bok	-20.20	188.74	43.03	8.05	0.02	0.25	11.68	31.5	6.3	25.1	79.9
91 Newcomb	29.76	43.65	39.80	8.05	0.03	0.23	6.37	53.2	5.8	47.4	89.0
92 Seyfert	29.20	114.17	109.79	8.05	0.03	0.25	5.83	44.4	17.4	27.0	60.7
93 crater_04	4.45	159.78	52.09	8.05	0.03	0.24	4.02	51.5	7.8	43.7	84.9
94 Manilius	14.43	9.05	37.82	8.05	0.02	0.22	6.70	51.7	5.5	46.2	89.3
95 crater_15	16.27	173.84	46.70	8.05	0.03	0.25	4.28	24.7	6.9	17.8	72.0
96 Zernike	18.27	168.24	49.46	8.05	0.02	0.25	4.28	38.2	7.4	30.9	80.7
97 Lobachevskiy	9.82	113.27	87.69	8.04	0.02	0.29	7.34	40.1	13.7	26.4	65.9
98 crater_32	7.16	168.72	37.74	8.04	0.02	0.27	4.84	48.4	5.5	42.9	88.6
99 Ellerman	-25.56	239.50	46.21	8.04	0.04	0.22	6.04	64.0	6.8	57.2	89.3
100 Lowell	-13.01	256.63	62.65	8.04	0.04	0.31	7.42	68.5	9.5	59.0	86.1
101 Crookes	-10.35	194.86	49.65	8.03	0.02	0.30	5.36	64.9	7.4	57.5	88.6
102 Sniadecki	-22.33	191.33	41.13	8.03	0.02	0.21	5.43	22.2	6.0	16.2	72.8
103 crater_24	-16.61	112.33	45.89	8.03	0.03	0.00	0.00	59.9	6.8	53.1	88.7
104 Harvey	19.37	213.42	59.98	8.03	0.03	0.24	5.44	66.3	9.1	57.3	86.3
105 Eichstadt	-22.65	281.62	50.10	8.03	0.04	0.24	6.44	46.1	7.5	38.6	83.8
106 Mach	18.12	210.89	187.61	8.02	0.02	0.22	5.10	48.5	31.1	17.4	35.9
107 Alter	18.71	252.12	64.73	8.02	0.02	0.22	5.34	42.6	9.8	32.7	76.9
108 Plutarch	24.12	79.00	69.59	8.02	0.04	0.27	4.23	45.1	10.7	34.5	76.4
109 Poynting	17.59	226.57	128.76	8.02	0.07	0.22	5.20	58.0	20.7	37.3	64.3
110 Bronk	25.91	225.23	61.58	8.02	0.02	0.23	4.90	54.7	9.3	45.4	82.9
111 Holetschek	-27.81	151.21	38.88	8.01	0.03	0.22	5.69	46.8	5.7	41.1	87.9
112 Aitken	-16.66	173.25	137.94	8.01	0.07	0.24	4.61	41.1	22.3	18.8	45.8
113 Gassendi	-17.50	320.02	109.58	8.00	0.04	0.23	7.07	42.1	17.4	24.8	58.7
114 crater_43	14.91	163.64	48.56	8.00	0.04	0.24	4.27	54.6	7.2	47.4	86.8
115 Joule	27.17	215.84	97.52	7.99	0.03	0.26	3.85	60.2	15.3	44.9	74.5
116 Jackson	22.00	196.75	71.75	7.99	0.04	0.38	6.73	64.9	11.0	53.9	83.1
117 crater_16	17.39	277.83	45.86	7.99	0.03	0.23	4.86	36.5	6.8	29.7	81.4
118 Piccolomini	-29.74	32.16	87.58	7.99	0.05	0.24	4.29	53.6	13.7	40.0	74.5
119 Ohm	18.30	246.24	62.95	7.99	0.04	0.30	8.78	54.9	9.6	45.3	82.6
120 Golitsyn	-25.21	254.88	32.72	7.97	0.05	0.25	5.74	54.5	4.7	49.8	91.4
121 crater_20	26.61	182.97	38.01	7.97	0.02	0.27	4.14	53.2	5.5	47.7	89.6
122 Sharonov	12.35	173.17	78.16	7.95	0.05	0.29	4.29	42.6	12.1	30.5	71.6
123 King	5.04	120.43	77.55	7.95	0.03	0.37	8.58	49.3	12.0	37.3	75.7
124 Robertson	21.82	254.63	89.85	7.94	0.04	0.27	5.57	39.0	14.0	25.0	64.0
125 Langemak	-9.90	119.46	105.32	7.94	0.03	0.27	5.99	50.7	16.7	34.0	67.1
126 Buys_Ballot	20.81	174.71	66.38	7.93	0.04	0.26	3.82	17.5	10.1	7.3	42.0
127 crater_37	-27.27	231.94	32.21	7.93	0.03	0.23	5.56	83.7	4.6	79.1	94.5
128 Alphonius	-13.38	357.10	110.54	7.89	0.03	0.26	3.62	54.3	17.6	36.8	67.7
129 Bullialdus	-20.74	337.64	60.72	7.87	0.04	0.37	10.92	30.4	9.2	21.2	69.8
130 Virtanen	15.83	176.91	44.58	7.86	0.04	0.34	2.86	33.1	6.6	26.6	80.1
131 Izsak	-23.33	117.55	31.32	7.85	0.03	0.26	5.31	51.1	4.5	46.6	91.2
132 Petavius	-25.42	60.76	184.06	7.84	0.05	0.00	0.00	45.8	30.4	15.4	33.6
133 Olcott	20.39	117.54	79.94	7.83	0.06	0.31	3.74	38.4	12.4	26.1	67.8
134 Kepler	8.09	321.98	29.49	7.81	0.10	0.32	13.11	42.7	4.2	38.4	90.1
135 Aristarchus	23.74	312.50	39.99	7.70	N.A.	0.41	6.26	34.9	5.9	29.1	83.2

^aClementine-derived OMAT and FeO abundance are averaged over the same area that the CF value was sampled. Crustal thickness from Wieczorek et al. [2006]. Central peak depth of origin is $0.109D^{1.08}$, where D is crater diameter [Cintala and Grieve, 1998].

The M³ data were utilized to distinguish between the presence of olivine and pyroxene, as both of these minerals have moderately long CF positions. The M³ instrument has 86 spectral channels between 0.42 and 3.0 μm with spectral sampling of 0.04 μm , and the data used in this study was limited to global measurement mode with a spatial resolution of \sim 140 m/pixel (available from the Planetary Data System (PDS) [pds.jpl.nasa.gov]).

[46] Level 1B radiance data from M³ were converted to I/F [Besse et al., 2011] with the solar spectrum provided in the PDS. The continuum slope between the 0.66 and 1.938 μm bands was removed with a simple linear correction for better interpretability of 1–2 μm spectral features.

[47] The M³ spectral data were directly compared to laboratory spectra of olivine and pyroxene [Bishop et al., 1995; Mustard and Pieters, 1989], but another method was needed to better visualize the distribution of mafic minerals. Therefore, we developed olivine index map developed for this study based upon the integrated band depth (IBD) of olivine and pyroxene absorption features:

[48] A typical olivine spectrum is characterized by a broad composite absorption feature centered near 1.05 μm followed by a relatively featureless spectrum near 2 μm , while typical pyroxene spectra have two strong absorption features centered near both 1 and 2 μm (Figure 7). A ratio of the 1 μm feature IBD with the 2 μm feature IBD sharply distinguishes the presence of olivine from pyroxene and is the value used for our olivine index maps. The method developed to create the index image is shown in Figure 7, where first the continuum line bounding the absorption band for each feature is approximated by finding the maximum reflectance value within a small range of wavelengths at both ends of the absorption feature. The difference between measured reflectance and the continuum reflectance is summed across all bands inside the absorption feature, and the 1 μm IBD map is divided by the 2 μm map to highlight regions with strong olivine spectral signatures.

[49] Band-independent noise in the form of vertical streaks is prevalent in M³ band ratio images, and a frequency domain filter was applied to the olivine index map to improve image quality. The single pixel wide near-vertical noise can be isolated and removed with a horizontal notch reject filter applied in the frequency domain [Castleman, 1996]. This desstriping method improves image quality and interpretability in band ratio images.

[50] Central peak CF values were also compared with 1 ppm sampling crustal thickness data presented in Wieczorek et al. [2006]. The data used in this study, Model 2, is a single-layer crustal thickness model with minimum crustal thickness of nearly 0 km beneath the Apollo basin and a maximum thickness of about 104 km. Other versions of this model showed no change in the interpretation of our results.

[51] The depth of origin for uplifted central peak material is a function of crater diameter as described by Cintala and Grieve [1998], where the minimum depth of origin is coincident with the maximum depth of melting. Given a crater diameter, D in kilometers, the depth of origin is $0.109D^{1.08}$. As shown in Cahill et al. [2009], the proximity of the central peak's depth of origin (D_{cp}) to the crust-mantle boundary (T , crustal thickness) in kilometers is $T - D_{\text{cp}}$. Expressed in terms of percentage of the total crustal column (peak origin

normalized to crustal thickness), $(T - D_{\text{cp}}) / T \times 100\%$ is the proportion of crustal material that is at a greater depth than the depth of origin for the uplifted central peak material.

3. Results

3.1. Distribution of Central Peak Compositions

[52] Based upon our survey of central peak compositions for 135 craters within 30° latitude of the equator (Table 2), 53% of craters have a central peak CF value below 8.10 μm , which is indicative of predominantly plagioclase-rich compositions. The mean CF value for all craters is 8.10 μm with a maximum of 8.48 μm (Eratosthenes crater) and a minimum of 7.70 μm (Aristarchus crater). Note that the sample size for highlands craters makes up a much larger proportion of the all craters sampled (105 of 135) than craters in the mare (30 of 135), so the compositional distribution of mare craters may not be as representative of the population as that of highlands craters that were analyzed.

[53] Central peak CF values were binned from 7.6 to 8.56 μm at increments of 0.04 μm to produce a histogram (Figure 8a). The distribution is bimodal with peaks at 8.08 and 8.16 μm .

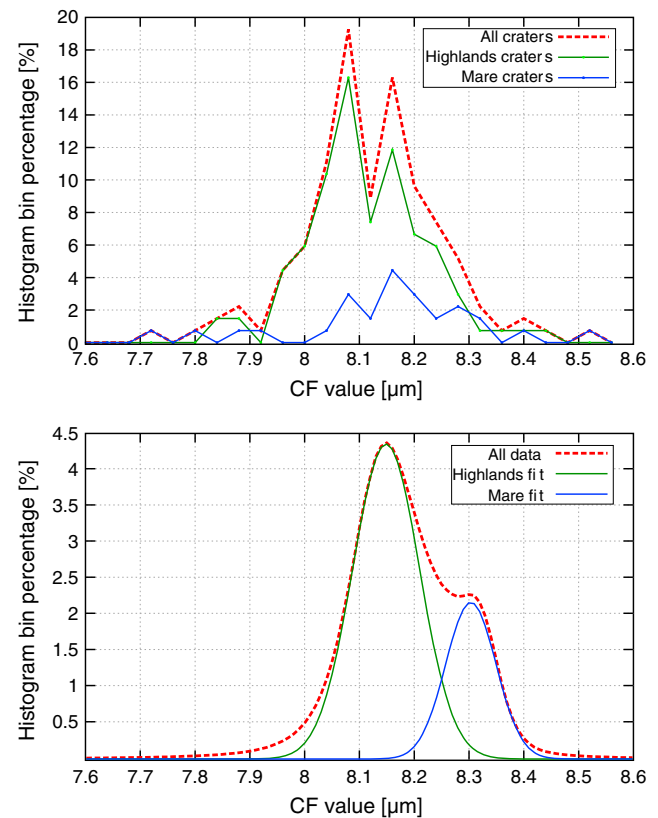


Figure 8. (a) CF value distributions for crater central peaks from this study and (b) a global compositional study of CF values from Greenhagen et al. [2010]. The central peak histogram (Figure 8a) shows the distribution of CF values for all 135 craters (dashed line). CF values are binned in 0.04 μm increments from 7.6 to 8.56 μm . The distribution is bimodal, with maxima at CF values of 8.08 and 8.16 μm . The global histogram (Figure 8b) also shows a bimodal distribution (dashed line) with the modal mean of highlands terrain at 8.15 μm and mare terrain at 8.3 μm .

The 8.08 μm peak (CF values between 8.04 and 8.08 μm) is made up of 19% of the surveyed craters, 21% of the highlands craters, and 13% of the mare craters. The longer wavelength 8.16 μm peak holds 16% of all craters, representing 15% of the highlands craters and 20% of the mare craters. Based on the global CF value histogram from *Greenhagen et al.* [2010] (Figure 8b), the variety and range of central peak silicate compositions is similar to those found globally on the surface of the Moon, although shifted to slightly shorter wavelengths by $\sim 0.1 \mu\text{m}$.

[54] The CF value of crater central peaks is not strongly correlated with local crustal thickness, central peak depth of origin, or depth of origin relative to the crust-mantle boundary (Figure 9). For example, Humboldt crater (199.5 km diameter) has multiple central peaks that are composed of uplifted material from the lower crust, only ~ 2 km from the crust-mantle interface according to our simple uplift model. However, the CF value of 8.08 μm measured in the central peak of Humboldt crater shows little evidence of mantle-like

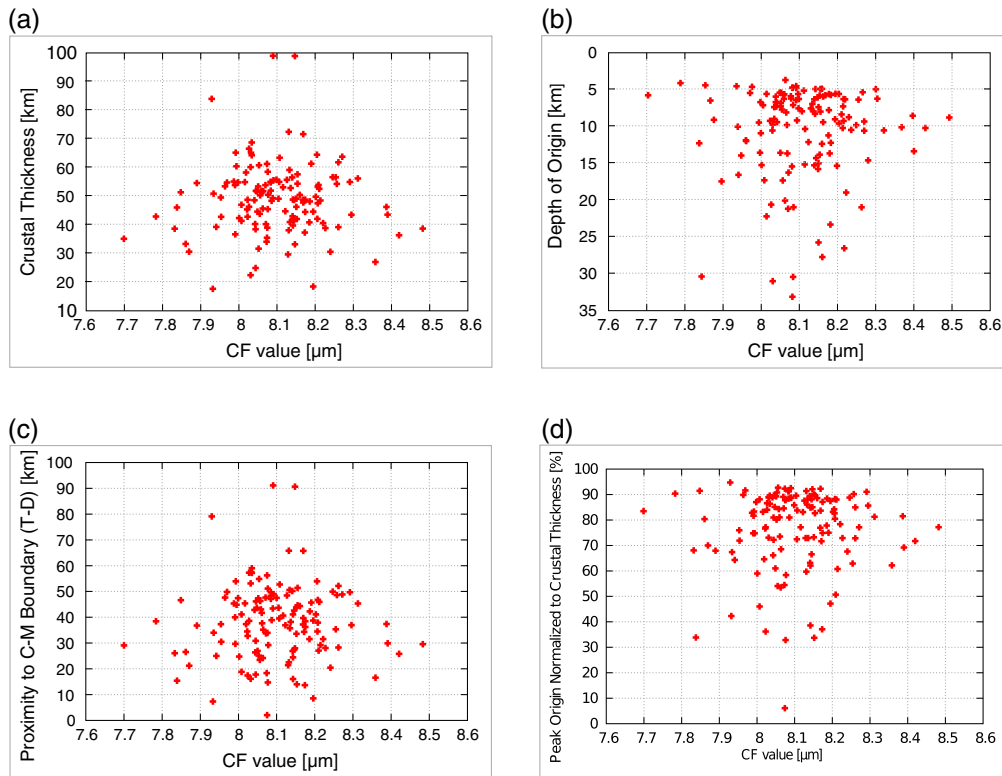


Figure 9. Comparison of central peak CF values with crustal depth. (a) Crustal thickness (km). (b) Central peak depth of origin (km). (c) Proximity of uplifted material to crust-mantle interface (km). (d) Peak origin normalized to crustal thickness (%). Proximity of uplifted material to crust-mantle surface (Figure 9c) is crustal thickness minus depth of origin, and Figure 9d is this same value as Figure 9c but divided by crustal thickness to show relative positions in the crustal column.

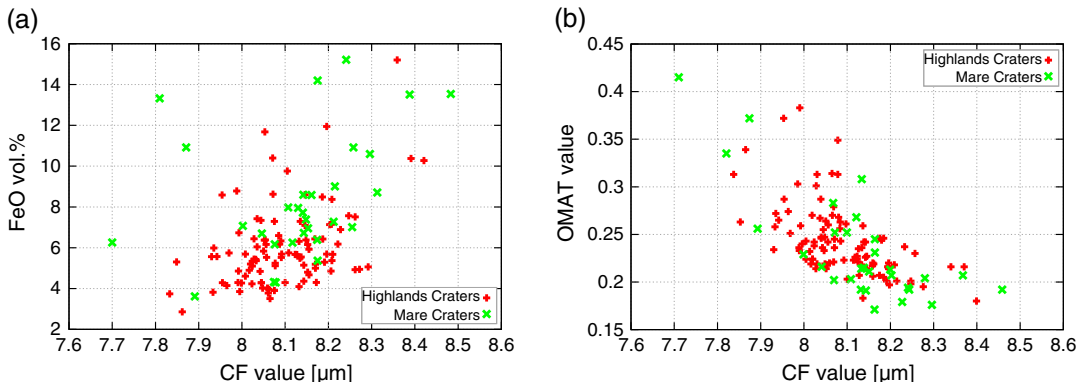


Figure 10. (a) Clementine-derived FeO abundance and (b) OMAT maturity parameter versus CF value.

mafic material and is more consistent with an anorthositic composition.

[55] Central peak CF values appear to be correlated with Clementine-derived FeO abundance and OMAT values (Figure 10), though the correlation is stronger with OMAT than FeO abundance. Longer-wavelength CF values, indicative of high proportions of mafics relative to plagioclase, correspond weakly to higher abundances of FeO (Figure 10a). Seventy-two percent of the central peaks have an FeO abundance between 4 and 8 wt.%, where the CF value ranges between 7.85 and 8.29 μm (excluding Aristarchus crater, where the CF value is approximate). Craters with central peaks that are more optically weathered (low OMAT value) show higher CF values than less weathered central peaks (Figure 10b).

[56] Only six craters (4%) were found with CF values above the average global mare CF value of 8.3 μm [Greenhagen et al., 2010]—Eratosthenes, Taruntius, Gutenberg craters within the nearside mare and Plummer, Scaliger, and Barringer craters in the farside highlands. Although many of the more feldspathic CF values were found in highlands craters, the two lowest CF values were located on the nearside mare in the central peaks of Aristarchus and Kepler craters. Both of these craters are in Procellarum basin where the crust can be more than 10 km thinner than in the highlands.

3.2. Regional Central Peak Compositions

3.2.1. Mare Crater Compositions

[57] Craters within the mare show a wide range of compositions in their central peaks (Figure 8a). Although the sample size of the mare craters is much smaller than the highlands craters, mare crater central peaks contain some of the more extreme CF values found in this study including the most mafic and most silicic compositions. Thirty percent of the mare craters have central peak CF values below 8.1 μm , and 60% have central peak CF values between 8.1 and 8.3 μm . The modal mean CF value for mare craters, based on the 0.04 μm bin histogram, is 8.16 μm .

[58] The central peak with the most mafic CF value is in the ~59 km diameter Eratosthenes crater (348°E , 14.5°N), along the southern rim of Imbrium basin. The average CF value of the mafic exposure in the central peak is 8.48, which is between the CF positions of pure pyroxene (8.25 μm) and olivine/forsterite (8.67 μm) [Donaldson Hanna et al., 2012; Greenhagen et al., 2010], suggesting an olivine-rich composition with a small proportion of pyroxene or a smaller proportion of plagioclase. The feature is on the eastern leg of the central peak (Figure 11) along a relatively constant slope with no dramatic topographic changes.

[59] Average Clementine-derived FeO abundance in this feature is 15.2 wt.%, and average OMAT value is 0.23 (close to the average central peak maturity determined in this study, 0.24). The crust is ~39 km thick in this location, and the estimated depth of origin for peak material is ~9 km below the surface, which is far removed from the crust-mantle boundary.

[60] Taruntius crater is another example of a crater with a mafic central peak composition. Taruntius is a 57 km

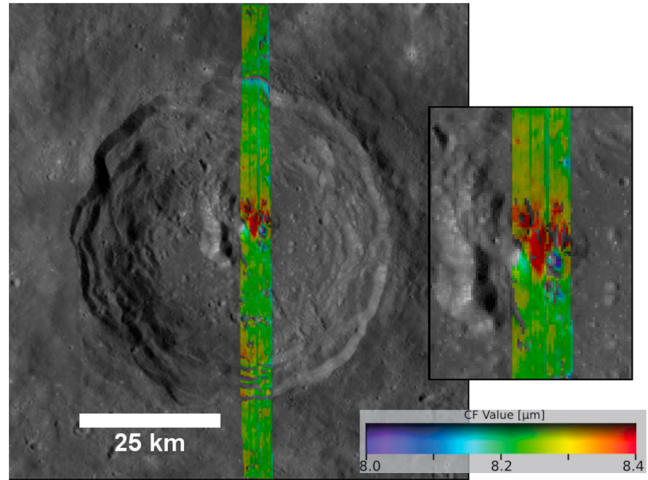


Figure 11. Eratosthenes crater, two orbits of data shown as colorized CF value (8.0–8.4 μm stretch) over LROC WAC basemap. Close-up of central peak on the right.

diameter crater on the northwest rim of Mare Fecunditatis (just east of Mare Tranquillitatis and south of Crisium at 46.5°E , 5.5°N). The CF value in its peak is 8.39 μm , and its proportion of mafics to plagioclase is higher than that of typical mare basalts. Average FeO abundance is 13.5 wt.%, and OMAT is 0.21 (slightly more weathered than average central peaks, but less than typical Mare basalts). Crustal thickness at this location is 46 km with an estimated central peak depth of origin of ~9 km.

[61] Aristarchus crater in the center of Oceanus Procellarum has shown evidence of silicic magmatism exposed in the crater and its rays [Glotch et al., 2010]. The central peak appears to be extremely silicic, with a concave-up 3-point Diviner spectrum that prevents usage of the parabolic interpolation method to derive the CF value. Based on the results of Glotch et al. [2010], we approximate the upper limit of the central peak CF value to be ~7.70 μm . Clementine-derived FeO abundance of 6.3 wt.% at the central peak is about half that of typical mare basalt.

[62] Kepler crater, also in Procellarum basin ~ 20° to the south of Aristarchus crater, shows a central peak CF value of 7.81 μm . The 3-point Diviner spectrum is concave downward, and the CF value is definable. The sampled region contains about 13.1 wt.% FeO, which is similar to the surrounding mare basalt. Kepler crater is relatively small (29.5 km diameter), so the material in its central peak originated from only ~4 km into the crust—potentially near the boundary between the mare basalt lens and the original anorthositic crust. However, the low CF value indicates a composition significantly more felsic than typical anorthositic highlands.

[63] Copernicus is a 96 km diameter crater in Insularum basin with central peaks originating from ~15 km below the surface into a ~40 km thick crust. This is the only crater found in this study that shows unambiguous evidence of a mafic exposure in its crater walls (Figure 12). Its centermost peak shows a relatively felsic average CF value of 8.14 μm similar to highlands terrains, while the crater

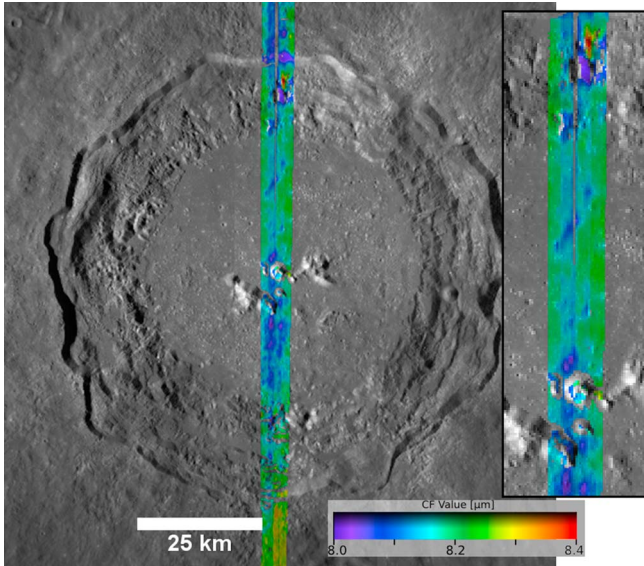


Figure 12. Copernicus crater, two orbits of data shown as colorized CF value (8.0–8.4 μm stretch) over LROC WAC basemap. Close-up of central peak and north crater wall feature.

wall feature has a more mafic CF value of 8.33 μm . The center-most peak OMAT is 0.31, indicating a relatively young surface exposure that could partially account for the unusually low central peak CF value. The wall feature is closer to average central peak optical maturity with an OMAT of 0.24. Clementine-derived FeO abundance is a relatively low 6.7 wt.% in the center-most peak, while the wall feature has 10.1 wt.% FeO.

[64] The wall feature is approximately 2.5 km long and 0.9 km wide and located just below the top of the first terrace from the northern crater rim. The shape and breadth of the wall feature indicates that the CF value of the feature is representative of a compositional variation rather than a temperature-dependent shift. *Lucey et al.* [1991] noted this feature as olivine-rich and pyroxene-poor using telescopic

multispectral NIR data. High-resolution LROC NAC imagery (M127063668R) shows a dark-toned region that coincides with the mafic crater wall CF feature (Figure 13). The area appears to be overlapping or surrounded by several small craters or pits.

3.2.2. Highlands Crater Compositions

[65] Highlands crater central peaks show a wide range of compositions much like the mare craters. Craters with the most mafic central peak CF values (Plummer, Scaliger, Barringer) are found near the rims of small farside basins (Milne and Apollo, near SPA basin). Fifty-six percent of the highlands craters have central peak CF values between 7.9 and 8.1 μm , and most highlands craters show central peak compositions consistent with mafics/plagioclase ratios similar to that of the anorthositic highlands. Thirty-nine percent of the highlands craters have CF values between 8.1 and 8.3 μm , implying that many of the highlands craters are uplifting material with mafics/plagioclase ratios similar to that of mare basalt.

[66] Plummer and Barringer craters near the northern rim of South Pole–Aitken basin have average central peak CF values of 8.42 and 8.36 μm , respectively. The central peak Clementine-derived FeO abundance is 10.3 wt.% for Plummer crater. Although Barringer crater has a slightly lower CF value, it has a derived 15.2 wt.% FeO in its central peak. Due to their proximity to South Pole–Aitken basin, the crustal thickness is relatively low for these craters, with Plummer crater uplifting material from ~26 km depth with a 31 km thick crust and Barringer crater uplifting from ~17 km into the 27 km thick crust.

[67] Olcott crater (20.4°N, 117.5°E) is an 80 km diameter crater with the most feldspathic central peak in the highlands, with a CF value of 7.83 μm . The central peak is less weathered than the average central peak with an OMAT value of 0.31 and shows a very low FeO abundance of 3.73 wt.%. Crustal thickness is relatively low where Olcott is located (38 km), and the material being uplifted in its central peak is from ~12 km depth, above ~68% of the crustal column.

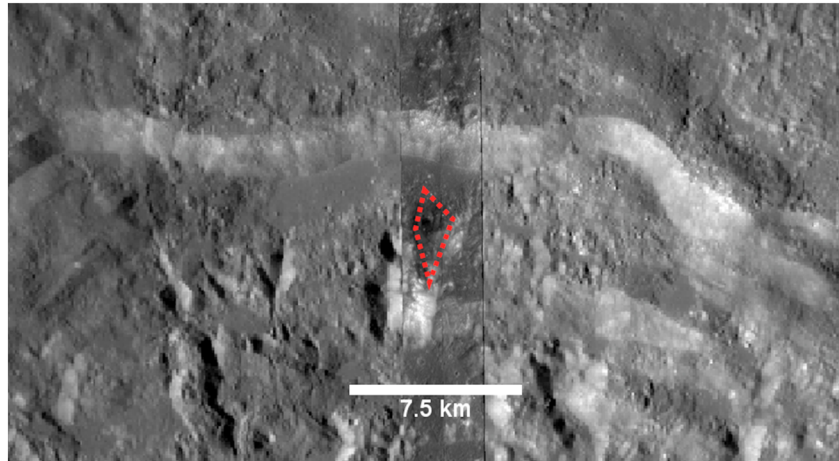


Figure 13. LROC NAC image (M127063668R) over the northern wall CF feature. Dotted red shape shows approximate boundary of CF feature.

4. Discussion

4.1. Global Composition

4.1.1. Histogram

[68] The histogram of CF values from our central peak survey shows two maxima at CF values of 8.08 and 8.16 μm that represent the most frequently occurring peak compositions (Figure 8a). The highland and mare crater CF wavelength distributions are skewed toward their respective histogram peaks but are not distinctly split into two separate populations. The global CF distribution from *Greenhagen et al.* [2010] shows the modal mean CF values for the mare (8.3 μm) and highlands (8.15 μm) terrains. The maximum in the central peak CF distribution occurs at shorter wavelengths than the global CF distribution, which can be primarily attributed to the fact that central peaks tend to be less optically mature than surrounding terrain due to their steep slopes that experience mass wasting processes. As described earlier with the Reiner Gamma case, the CF position shifts shortward up to $\sim 0.1 \mu\text{m}$ with less mature surfaces and can account for much of the difference between the global and central peak CF distributions.

[69] The similarity between the global CF distribution from *Greenhagen et al.* [2010] and our central peak CF distribution implies that the bulk SiO_2 content of uplifted material found in the central peaks is not significantly different from the range of compositions found on the lunar surface. This does not imply that crustal composition is uniform with depth, however, as many craters in the highlands have central peaks that have a similar mafics/plagioclase ratio to mare basalt, and some of the most felsic central peaks with the lowest CF values are located in the maria. The similarity may also be the result of various weathering processes (e.g., regolith formation) that could effectively homogenize surface compositions at both global and local scales (although mass wasting would reverse this).

[70] There is a prominent dip between the maxima in the central peaks histogram, suggesting that intermediate compositions between the two maxima occur less frequently in central peaks. About 31% of highlands craters and 53% of mare craters have central peaks with CF values between 8.15 and 8.3 μm , indicating that a significant portion of the central peak material has mafic compositions with similar mafics/plagioclase ratios as mare basalts, regardless of surface terrain.

4.1.2. CF Values Compared to FeO , OMAT

[71] The CF value appears to be correlated with Clementine-derived FeO abundance and optical maturity. (Note that there are four craters in this survey that lacked Clementine 950 nm band data coverage so they are not included in this analysis—Langrenus, Petavius, Craters 24 and 33). The CF value generally increases with increasing FeO wt.% (Figure 10a), although Kepler crater in the Procellarum Basin is a notable outlier with a low-average central peak CF value of 7.81 μm and a relatively high 13.1 wt.% FeO . Rock compositions with less than 4 wt.% FeO are uncommon on the Moon, resulting in a 4% cutoff in the vertical axis.

[72] The CF value versus optical maturity parameter (OMAT) shows a negative trend (Figure 10b)—CF value decreases as OMAT increases (i.e., CF position increases with more mature surfaces). The CF value appears to vary

freely with older surfaces (lower OMAT value), ranging between 8.0 and 8.5 μm for surfaces older than the mean OMAT value for this data set (0.24). The CF value becomes more constrained with younger surfaces, decreasing linearly with increasing OMAT values. This CF value shift could be the result of compositional changes from increased surface exposure. Alternatively, the weathering-induced darkening of the surface could alter the vertical thermal gradient, which can shift the CF value. Continuing work on understanding the relationship between the CF value and optical maturity can help decouple the two in future studies.

4.1.3. CF Values Compared to Crustal Depth

[73] The CF value is not correlated with the depth of origin of the peak material (Figure 9). Central peak composition appears to be independent of the crust thickness (Figure 9a), peak depth of origin (Figure 9b), and the proximity of that depth of origin to the crust-mantle boundary (Figure 9c). This implies that craters that are likely uplifting deeply sourced crustal materials do not have central peak compositions significantly more mafic than those that are uplifting materials closer to the surface. Although a wide range of central peak compositions have been found, their depths of origin relative to the crust-mantle boundary do not show a clear felsic-to-mafic gradient that may have been expected according to lunar crustal formation models.

[74] Recent findings by *Pieters et al.* [2011] suggest alternate mechanisms that could have formed unusual lithologies within the crust that is not dependent on the depth at which they formed. Mineralogical analysis of M³ spectra by [Pieters et al., 2011] revealed small (approximately few kilometers), localized exposures of Mg-Al spinel alongside orthopyroxene and olivine in the inner ring of Moscovense. They identified five unusually homogeneous regions of spinel, orthopyroxene, and olivine-rich compositions that are distinct from each other as well as the highly anorthositic surrounding terrain. Unlike olivine and pyroxene, spinel does not form in silica-rich magma bodies and its presence in conjunction with these mafic silicates is highly unusual. The favored formation mechanism for these regions is endogenic—the formation of Moscovense basin could have uplifted and exposed mafic plutonic systems that had undergone fractional crystallization. The crystallization process would initially produce layers of olivine and pyroxene, depleting the silicate reservoir within the pluton and allowing the remaining Mg and Al to form spinel.

[75] *Gross and Treiman* [2011] supported these findings with the identification of a spinel-rich lunar meteorite with similar composition to the regions described by *Pieters et al.* [2011]. The clasts in the meteorite show a textural disequilibrium between the very fine-grained spinel and pyroxene, suggesting rapid cooling and low pressures during formation. This implies that the spinel-rich regions found by *Pieters et al.* [2011] may not have formed deep within the crust, and the formation of nonanorthositic compositions is not necessarily dependent on the proximity of the source melt to the mafic mantle.

[76] An additional source of evidence supporting our findings of globally distributed mafic-enhanced compositions is from lunar regolith breccia meteorites, which are consolidated samples of fine-grained lunar soil that fused together during impact events. A study of these meteorites by *Korotev et al.* [2009] has shown that they are of intermediate compositions

between feldspar (3%–7% FeO) and basalt (17%–23% FeO), like many of the central peaks from both highlands and mare terrain in our study. Joy *et al.* [2010] found several meteorites that are compositionally consistent with a cryptomaria source where mare basalt intrusions failed to reach the surface. These previous studies along with the results presented here support a heterogeneous and complex distribution of compositions within the lunar crust.

4.1.4. CF Values Compared to NIR-Derived Composition

[77] A comparison of central peak CF values to mineralogical abundances from Cahill *et al.* [2009] show no clear correlations between CF value and olivine, clinopyroxene, orthopyroxene, and plagioclase abundance derived from NIR multispectral data. Only 16 craters from their study overlapped with the ones investigated here, and exact locations sampled from the central peaks may differ between the two studies, preventing direct mineralogical comparisons. Olivine index images derived from M³ data show some correlations with high CF value regions (discussed below), though only two craters were analyzed with this method.

4.2. Local Composition

[78] Craters in the nearside maria showed the most unique and diverse compositions in their central peaks. Because mare craters are confined to a smaller surface area, the variety of compositions identified indicate a heterogeneous crust with regional variations, perhaps due to the presence of plutonic systems. Craters in this study exhibiting the lowest CF values in their central peaks (e.g., Aristarchus, Kepler) are located in the same nearside maria region as craters with some of the highest CF values (Eratosthenes, Taruntius). Aristarchus crater is located in a region covered in highly silicic compositions [Glotch *et al.*, 2010], which can account for the relatively low FeO abundance (~6.3 wt.%) and extremely low CF (<7.7 μm). Kepler crater, on the other hand, has a high FeO abundance (~13.1 wt.%) but an average CF value of 7.81 μm in its central peak. This could be due to the relatively small crater diameter of Kepler (29.5 km) that is around the transition diameter between simple and complex craters, resulting in an irregular and off-center peak that likely uplifted anorthositic crust just below the mare basalt lens. The disparity between the low CF value and high FeO abundance can only be partially explained by the contrast between the relatively unweathered central peak of Kepler, which would lower the CF value by ~0.1 μm . The FeO abundance is similar to typical mare basalts that have a CF value near 8.15 μm . It is possible that a slight misregistration between the Clementine and Diviner data sets can be responsible for this discrepancy.

[79] Out of the 135 craters surveyed, only six craters exhibit central peak compositions more mafic than average maria, with CF values greater than 8.3 μm . We can infer from this that ultramafic compositions are uncommon within the lunar crust and mantle-like compositions of pure olivine (CF value of 8.67 μm) are not being uplifted by complex craters.

[80] Eratosthenes crater shows a central peak CF value of 8.48 μm , indicative of an olivine-rich composition with small amounts of pyroxene and/or plagioclase. The CF value map (Figure 11) shows that the mafic exposure on the central peak of Eratosthenes is broad and sustained on both north and south facing slopes, indicating that the CF position is unaffected by temperature-dependent anomalies. The

olivine index image derived from M³ spectra (Figure 14a) shows a strong and extensive olivine feature on the eastern leg of the peak that is coincident with the Diviner high CF value feature, indicating a high abundance of olivine and relatively low abundance of pyroxene. Other prominent olivine features can be seen on a small region on the west leg of the peak as well as a large feature on the northeast outer crater wall. As shown in the scatterplot of olivine index versus CF value (Figure 15), there is good agreement between the two data sets and they both support the presence of high abundances of mafic materials in Eratosthenes crater.

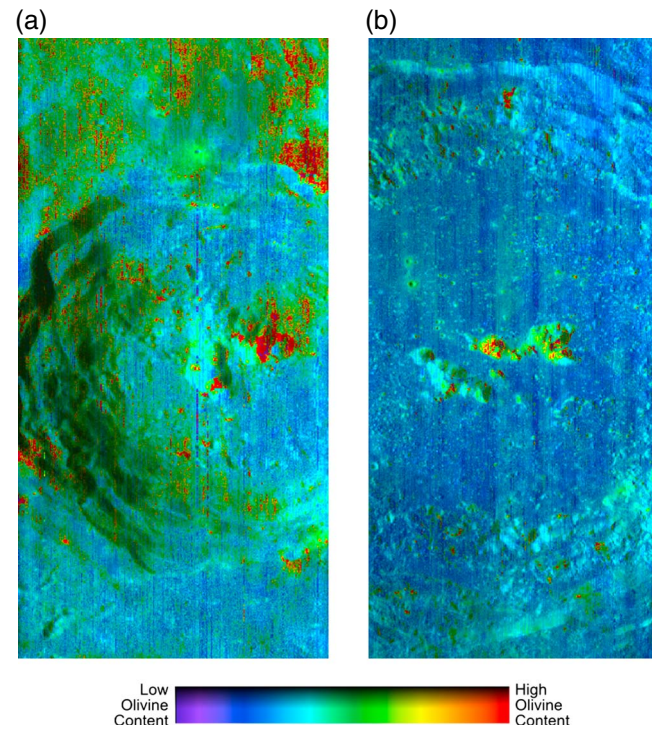


Figure 14. Olivine index maps derived from M³ reflectance spectra of Eratosthenes and Copernicus craters. Regions mapped in red have a strong 1 μm absorption feature and weak 2 μm absorption feature, characteristic of the presence of olivine. Olivine index (the ratio of 1 and 2 μm integrated band depths) is stretched from -1.5 to 4 and colorized, with an M³ channel 1 (0.46 μm) basemap. Images are unprojected, but both are ~40 km wide. (a) The central peak of Eratosthenes crater shows an extensive olivine feature on the eastern leg of the peak that overlaps with the high CF value feature (8.48 μm in the sampled region shown), indicating a high abundance of olivine and relatively low abundance of pyroxene. Other prominent olivine features can be seen on a small region on the west leg of the peak as well as a large feature on the northeast outer crater wall. (b) Copernicus crater generally shows lower olivine indices than Eratosthenes, with moderately strong olivine features on the center-most and eastern peaks. Average CF value of the center-most peak is 8.14 μm , which suggests a bulk composition rich in plagioclase with some olivine mixed in. The concentrated feature in the northern wall likely has a bulk composition with a higher proportion of olivine than the central peaks, with a corresponding CF value of 8.33 μm .

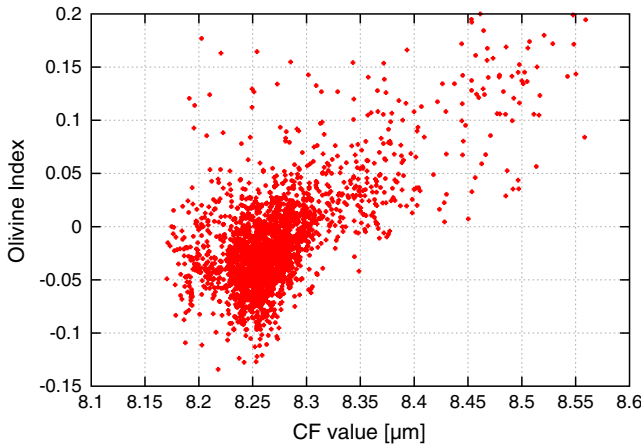


Figure 15. Scatter plot of olivine index derived from M^3 reflectance spectra versus Diviner CF value for Eratosthenes crater (Figures 11 and 14a). The olivine index increases with increasing CF value.

[81] Copernicus crater (Figure 12), reported in previous works to contain exposures of olivine-rich compositions in its central peaks [Cahill et al., 2009; Tompkins and Pieters, 1999; Yamamoto et al., 2010, among others], shows an average CF value of $8.14\text{ }\mu\text{m}$ at its center-most peak, consistent with a largely anorthositic composition with small amounts of mafics mixed in. The northern crater wall, however, shows a long exposure of more mafic material with an average CF value of $8.33\text{ }\mu\text{m}$. FeO abundance is 6.7 wt.% in the central peak and 10.1 wt.% in the northern wall feature, and both wall and peak features fall along the global central peak FeO versus CF trend shown in Figure 10. One possible source of unique crater wall compositions could be the ponds of impact melt that can be trapped on top of the terraces that are tilted outward from the center of the crater [Melosh, 1989]. The small craters or pits near the feature could be exposing the melt, allowing it to be distinguishable from the ubiquitous regolith.

[82] The olivine index image based on M^3 spectra of Copernicus crater (Figure 14b) show strong olivine features in both the central peaks and northern wall CF feature. Copernicus crater generally shows lower olivine indices in the M^3 data than Eratosthenes, with moderately strong olivine features on the center-most and eastern peaks. The northern wall feature seen in the CF value image coincides directly with the major olivine feature in the M^3 index image, and the rest of the crater wall shows several much smaller olivine features (particularly in the southeastern wall) that are not well resolved in the Diviner CF data. The center-most and eastern central peaks show clear evidence of olivine in the index image, which has no corresponding feature in the Diviner CF value imagery. This could imply that relatively small amounts of olivine are mixed into a predominantly plagioclase-rich composition, resulting in a felsic bulk composition with a CF value between 8.1 and $8.2\text{ }\mu\text{m}$ and moderately low FeO content around 7 wt.%.

4.3. Implications

[83] Most of the uplifted mafic material found in central peaks indicates a mafic component similar to mare basalt, which could be sourced from a mix of felspathic crust with

mafic plutons or cryptomaria. The CF position of pyroxene falls around $8.25\text{ }\mu\text{m}$ in simulated lunar conditions [Donaldson Hanna et al., 2012; Greenhagen et al., 2010], so it is possible (albeit unlikely) that the majority of the uplifted material (average CF of $8.1\text{ }\mu\text{m}$) is nearly pure pyroxene, rather than a mixture of plagioclase, pyroxene, and olivine. However, pyroxene is a cumulate crystallized in an intermediate environment along with olivine, so pure pyroxene rock is not likely to exist on the Moon in such abundance and it is much more likely that these central peaks are a mixture of all three minerals. The wide variety of compositions found in both mare and highlands crater central peaks indicates a great deal of inhomogeneity in the lunar crust. The extensive “plumbing” that transported mare basalt into the nearside basin could contribute to the wide range of compositions found in this study, particularly in the nearside maria.

[84] The lack of correlation between central peak CF values and crustal thickness could be primarily attributed to the Moon’s complex cratering history that constantly overturned the original crust’s stratigraphy. A possible scenario is that some of the impacts included in this study have uplifted stratigraphy that was previously overturned by impact events, so the stratigraphic sequence exposed in central peaks may be incoherently inverted. The outlier craters in the survey that have central peaks with very low or very high CF values may be examples of regional crustal variation (e.g., plutonic systems), whereas the bulk of the craters show a more homogenized crust due to previous impact events.

[85] A recent hypothesis from Jutzi and Asphaug [2011] suggests that the farside highlands are an accretionary pile from a small companion Moon colliding into the farside of the Moon at relatively low velocity (2–3 km/s). The companion Moon evolved more quickly than the Moon, with a crust and solid mantle but little to no core. The modeled collision is assumed to have occurred when the Moon’s magma ocean had largely solidified. The modeled hemispherical thickness of the accreted layer is consistent with the dimensions of the farside highlands. This is a possible cause—The collision of the companion Moon could have created a mixed intermediate layer between the accretionary pile and the Moon’s original farside surface, which could account for the wide variety of compositions found uplifted in highlands craters with no correlation to the peak’s depth of origin.

5. Conclusions

[86] Uplifted crustal material found in the central peaks of lunar craters show a vast compositional diversity in both mare and highlands terrain. The range of compositions is comparable to that found globally on the lunar surface, but the uplifted material is often not compositionally similar to the surrounding terrain. It is not uncommon for a crater in the highlands to uplift material that contains a similar amount of mafic material as typical mare basalt, which could be sourced from cryptomaria or mafic plutons that occur globally. Central peak compositions are not correlated with crustal thickness or the depth of origin for uplifted peak material. Copernicus crater has a relatively felsic CF value in its central peak compared to a mafic exposure in its

terraced northern wall, possibly composed of impact melt that has been exposed by small recent craters. Eratosthenes crater shows the strongest evidence of an ultramafic exposure in its central peak in both the CF value and M³-derived olivine index images.

[87] If the lunar crust had been compositionally stratified at some time, it is no longer the case. It is unclear from this work whether this compositional heterogeneity is due to a more complex origin than is described by simple models of cumulate formation or subsequent reworking via basin forming impacts or (as is likely) a combination of several processes. Regardless, this heterogeneity presents a challenge for understanding the details of lunar crustal formation and evolution.

[88] The combined use of NIR and thermal infrared spectral data sets provides complementary information that both supported and enhanced the interpretations presented here. FeO and optical maturity parameters provide additional valuable information that aids in the interpretation of the Diviner CF data. The M³ data provide a clear discriminability between pyroxene and olivine that can reduce the ambiguity in the interpretation of the mineralogy responsible for the CF position in the Diviner data. In addition, the Diviner CF measurements are highly sensitive to bulk mineralogy and can be used to constrain mineral abundances as determined by NIR spectral data sets.

[89] Future work that should be conducted includes corrections for the various noncompositional CF shifts in conjunction with the development of a topographic data set of similar resolution as Diviner data to increase the precision of the composition derived from CF values. Higher-resolution crustal thickness maps (e.g., from Kaguya data [Ishihara et al., 2009]) could improve comparisons between our bulk compositions and the depth of origin of uplifted material relative to the crust-mantle boundary. With the ever-increasing data coverage from Diviner, it will be possible to sample more than one region on the central peaks, which will provide a better understanding of compositional variation within a given crater.

[90] **Acknowledgments.** We would like to thank the Diviner science and operations teams at UCLA and Jet Propulsion Laboratory for their support. Thanks also to Jean-Pierre Williams at UCLA for developing data processing scripts that were vital for this project, Mark Sullivan at UCLA for technical support. Many thanks to Alan Gillespie and Bruce Nelson at University of Washington for feedback and advice. Finally, thanks to Joshua T. Cahill and an anonymous reviewer for their time and constructive advice that led to the publication of this manuscript.

References

- Bandfield, J. L. (2009), Effects of surface roughness and graybody emissivity on Martian thermal infrared spectra, *Icarus*, 202(2), 414–428. doi:10.1016/j.icarus.2009.03.031.
- Bandfield, J. L., R. R. Ghent, A. R. Vasavada, D. A. Paige, S. J. Lawrence, and M. S. Robinson (2011a), Lunar surface rock abundance and regolith fines temperatures derived from LRO Diviner Radiometer data, *J. Geophys. Res.*, 116, 1–18. doi:10.1029/2011JE003866.
- Bandfield, J. L., P. O. Hayne, R. R. Ghent, B. T. Greenhagen, and D. A. Paige (2011b), Lunar surface roughness and anisothermality effects on infrared measurements, in *Lunar and Planetary Science Conference*, vol. 42, p. 2468.
- Basaltic Volcanism Study Project (BVSP) (1981), Basaltic Volcanism on the Terrestrial Planets, p. 577, Pergamon Press, Inc., New York.
- Besse, S., J. M. Sunshine, M. I. Staid, and N. E. Petro (2011), Compositional variability of the Marius Hills volcanic complex from the Moon Mineralogy Mapper (M3), *J. Geophys. Res.*, 116, 1–15. doi:10.1029/2010JE003725.
- Bishop, J. L., C. M. Pieters, R. G. Burns, and J. O. Edwards (1995), Reflectance spectroscopy of ferric sulfate-bearing montmorillonites as Mars soil analog materials, *Icarus*, 117(1), 101–119.
- Cahill, J., and P. Lucey (2007), Radiative transfer modeling of lunar highlands spectral classes and relationship to lunar samples, *J. Geophys. Res.*, 112(E10).
- Cahill, J. T. S., P. G. Lucey, and M. A. Wieczorek (2009), Compositional variations of the lunar crust: Results from radiative transfer modeling of central peak spectra, *J. Geophys. Res.*, 114(E9), 1–17. doi:10.1029/2008JE003282.
- Castleman, K. R. (1996), *Digital Image Processing*, 2nd edition, pp. 275–277, Prentice Hall, Upper Saddle River, N. J.
- Cintala, M. J., and R. A. F. Grieve (1998), Scaling impact melting and crater dimensions: Implications for the lunar cratering record, *Meteorit. Planet. Sci.*, 33(4), 889–912. doi:10.1111/j.1945-5100.1998.tb01695.x.
- Colwell, J. E., and B. M. Jakosky (2002), Effects of topography on thermal infrared spectra of planetary surfaces, *J. Geophys. Res.*, 107(E11), 1–6. doi:10.1029/2001JE001829.
- Cooper, B. L., J. W. Salisbury, R. M. Killen, and A. E. Potter (2002), Midinfrared spectral features of rocks and their powders, *J. Geophys. Res.*, 107(E4). doi:10.1029/2000JE001462.
- Dhingra, D., C. M. Pieters, J. W. Boardman, J. W. Head, P. J. Isaacson, and L. A. Taylor (2011), Compositional diversity at Theophilus Crater: Understanding the geological context of Mg-spinel bearing central peaks, *Geophys. Res. Lett.*, 38(11). doi:10.1029/2011GL047314.
- Donaldson Hanna, K., M. B. Wyatt, I. R. Thomas, N. E. Bowles, B. T. Greenhagen, A. Maturilli, J. Helbert, and D. A. Paige (2012), Thermal infrared emissivity measurements under a simulated lunar environment: Application to the Diviner Lunar Radiometer experiment, *J. Geophys. Res.*, 117(V), 1–15. doi:10.1029/2011JE003862.
- Estep-Barnes, P. A. (1977), Infrared spectroscopy, in *Physical Methods in Determinative Mineralogy*, pp. 529–603, Academic Press, New York.
- Glotch, T. D. et al. (2010), Highly silicic compositions on the Moon, *Science*, 329(5998), 1510–3. doi:10.1126/science.1192148.
- Glotch, T. D., B. T. Greenhagen, and P. G. Lucey (2012), Observations of lunar swirls by the Diviner Lunar Radiometer experiment, in *Lunar and Planetary Science Conference*.
- Greenhagen, B. T. et al. (2010), Global silicate mineralogy of the Moon from the Diviner Lunar Radiometer, *Science*, 329(5998), 1507–9. doi:10.1126/science.1192196.
- Grieve, R. A. F. (1981), Impact cratering, *Nature*, 291, 16.
- Grieve, R. A. F., and P. B. Robertson (1979), The terrestrial cratering record: I. Current status of observations, *Icarus*, 38, 212–229.
- Gross, J., and A. H. Treiman (2011), Unique spinel-rich lithology in lunar meteorite ALHA81005: Origin and possible connection to M3 observations of the farside highlands, *J. Geophys. Res.*, 116, 1–9. doi:10.1029/2011JE003858.
- Hapke, B. (1996), Applications of an energy transfer model to three problems in planetary regoliths: The solid-state greenhouse, thermal beaming, and emittance spectra, *J. Geophys. Res.*, 101(E7), 16833–16.
- Heiken, G. H., D. T. Vaniman, and B. M. French (1991), *Lunar Sourcebook: A User's Guide to the Moon*, pp. 62–93, 610–632, Cambridge Univ. Press, Cambridge, U. K.
- Henderson, B. G., and B. M. Jakosky (1994), Near-surface thermal gradients and their effects on mid-infrared emission spectra of planetary surfaces, *J. Geophys. Res.*, 99(E9), 19063–19073. doi:10.1029/94JE01861.
- Henderson, B. G., and B. M. Jakosky (1997), Near-surface thermal gradients and mid-IR emission spectra: A new model including scattering and application to real data, *J. Geophys. Res.*, 102(E3), 6567–6580.
- Hörz, F., R. A. F. Grieve, G. H. Heiken, P. Spudis, and A. B. Binder (1991), Lunar surface processes, in *Lunar Sourcebook: A User's Guide to the Moon*, edited by G. H. Heiken, D. T. Vaniman, and B. M. French, pp. 61–120, Cambridge University Press, Cambridge, U. K.
- International Astronomical Union (IAU) Working Group for Planetary System Nomenclature (WGPSN) (n.d.), Gazetteer of Planetary Nomenclature, [online] Available from: <http://planetarynames.wr.usgs.gov/>
- Ishihara, Y., S. Goossens, K. Matsumoto, H. Noda, H. Araki, N. Namiki, H. Hanada, T. Iwata, S. Tazawa, and S. Sasaki (2009), Crustal thickness of the Moon: Implications for farside basin structures, *Geophys. Res. Lett.*, 36(19), 1–4. doi:10.1029/2009GL039708.
- Jolliff, B. L., and L. A. Haskin (1995), Cogenic rock fragments from a lunar soil: Evidence of a ferroan noritic-anorthosite pluton on the Moon, *Geochim. Cosmochim. Acta*, 59(11), 2345–2374.
- Jolliff, B. L., M. A. Wieczorek, C. K. Shearer, and C. R. Neal (Eds) (2006), *New Views of the Moon*, pp. 365–518, 519–596, Mineralogical Society of America, Chantilly, Va.
- Joy, K. H., I. A. Crawford, S. S. Russell, and A. T. Kearsley (2010), Lunar meteorite regolith breccias: An in situ study of impact melt composition using

- LA-ICP-MS with implications for the composition of the lunar crust, *Meteorit. Planet. Sci.*, 45(6), 917–946. doi:10.1111/j.1945-5100.2010.01067.x.
- Jutzi, M., and E. Asphaug (2011), Forming the lunar farside highlands by accretion of a companion Moon, *Nature*, 476(7358), 69–72. doi:10.1038/nature10289.
- Kahle, A. B., F. D. Palluconi, and P. R. Christensen (1993), *Thermal Emission Spectroscopy: Applications to the Earth and Mars*, edited by C. M. Pieters, and P. A. J. Englert, pp. 99–120, Cambridge Univ. Press, Cambridge, U. K.
- Korotev, R. L., R. A. Zeigler, and B. L. Jolliff (2009), Compositional and lithological diversity among brecciated lunar meteorites of intermediate iron concentration, *Meteorit. Planet. Sci.*, 1322(9), 1287–1322.
- LAPST (Lunar and Planetary Sample Team) (1985), Horizons and Opportunities in Lunar Sample Science, *LPI Tech. Rpt 85-04*, Lunar and Planetary Institute, Houston, 32pp.
- Lawrence, D. J., W. C. Feldman, R. C. Elphic, R. C. Little, T. H. Prettyman, S. Maurice, P. G. Lucey, and A. B. Binder (2002), Iron abundances on the lunar surface as measured by the lunar prospector gamma-ray and neutron spectrometers, *J. Geophys. Res.*, 107(E12). doi:10.1029/2001JE001530.
- Lucey, P. G. et al. (2006), Understanding the lunar surface and space-Moon interactions, *Rev. Mineral. Geochem.*, 60, 83–220.
- Lucey, P. G., and B. T. Greenhagen (2012), Lunar mineral maps integrating thermal and near infrared multispectral imaging, in *Lunar and Planetary Science Conference*.
- Lucey, P. G., B. R. Hawke, and K. Horton (1991), The distribution of olivine in the crater Copernicus, *Geophys. Res. Lett.*, 18(11), 2133–2136.
- Lucey, P. G., D. Blewett, and G. J. Taylor (2000), Imaging of lunar surface maturity, *J. Geophys. Res.*, 105, 377–386.
- Lucey, P. G., D. A. Paige, B. T. Greenhagen, J. L. Bandfield, and T. D. Glotch (2010), Comparison of Diviner Christiansen Feature position and visible albedo: Composition and space weathering implications, in *Lunar and Planetary Science Conference*, vol. 111.
- Matsunaga, T. et al. (2008), Discoveries on the lithology of lunar crater central peaks by SELENE Spectral Profiler, *Geophys. Res. Lett.*, 35(23), 1–5. doi:10.1029/2008GL035868.
- Melosh, H. J. (1989), *Impact Cratering: A Geologic Process*, pp. 130–154, Oxford Univ. Press (Oxford Monographs on Geology and Geophysics, No. 11), New York.
- Mustard, J. F. et al. (2011), Compositional diversity and geologic insights of the Aristarchus crater from Moon Mineralogy Mapper data, *J. Geophys. Res.*, 116. doi:10.1029/2010JE003726.
- Le Mouélic, S., and Y. Langevin (2001), The olivine at the lunar crater Copernicus as seen by Clementine NIR data, *Planet. Space Sci.*, 49(1), 65–70. doi:10.1016/S0032-0633(00)00091-X.
- Le Mouélic, S., Y. Langevin, S. Erard, P. Pinet, S. D. Chevrel, and Y. Dayou (2000), Discrimination between maturity and composition of lunar soils from integrated Clementine UV-visible/near-infrared data: Application to the Aristarchus Plateau, *J. Geophys. Res.*, 105(E4), 9445–9455. doi:10.1029/1999JE001196.
- Lyon, R. J. P. (1965), Analysis of rocks by spectral infrared emission (8 to 25 microns), *Econ. Geol.*, 60(4), 717–736. doi:10.2113/gsecongeo.60.4.715.
- Mustard, J. F., and J. Hays (1997), Effects of hyperfine particles on reflectance spectra from 0.3 to 25 μm , *Icarus*, 125(1), 145–163. doi:10.1006/icar.1996.5583.
- Mustard, J. F., and C. M. Pieters (1989), Photometric phase functions of common geologic minerals and applications to quantitative analysis of mineral mixture reflectance spectra, *J. Geophys. Res.*, 94.
- Noble, S. K., C. M. Pieters, L. A. Taylor, R. V. Morris, C. C. Allen, D. S. McKay, and L. P. Keller (2001), The optical properties of the finest fraction of lunar soil: Implications for space weathering, *Meteorit. Planet. Sci.*, 36(1), 31–42. doi:10.1111/j.1945-5100.2001.tb01808.x.
- O’Keefe, J. D., and T. J. Ahrens (1993), Planetary Cratering Mechanics, *J. Geophys. Res.*, 98(E9), 17011–17028. doi:10.1029/93JE01330.
- Osinski, G. R., L. L. Tornabene, and R. A. F. Grieve (2011), Impact ejecta emplacement on terrestrial planets, *Earth Planet. Sci. Lett.*, 310(3–4), 167–181. doi:10.1016/j.epsl.2011.08.012.
- Paige, D. A. et al. (2009), The Lunar Reconnaissance Orbiter Diviner Lunar Radiometer experiment, *Space Sci. Rev.*, 150(1–4), 125–160. doi:10.1007/s11214-009-9529-2.
- Pieters, C. M. (1982), Copernicus crater central peak: Lunar mountain of unique composition, *Science*, 215(4528), 59.
- Pieters, C. M. (1986), Composition of the lunar highland crust from near-infrared spectroscopy, *Rev. Geophys.*, 24(3), 557–578.
- Pieters, C. M. et al. (2009), The Moon Mineralogy Mapper (M3) on Chandrayaan-1, *Curr. Sci.*, 96(4), 1–6.
- Pieters, C. M. et al. (2011), Mg-spinel lithology: A new rock type on the lunar farside, *J. Geophys. Res.*, 116. doi:10.1029/2010JE003727.
- Pinet, P., S. D. Chevrel, and P. Martin (1993), Copernicus: A regional probe of the lunar interior, *Science*, 260(5109), 797–801. doi:10.1126/science.260.5109.797.
- Robinson, M. S. et al. (2010), Lunar Reconnaissance Orbiter Camera (LROC) instrument overview, *Space Sci. Rev.*, 150(1–4), 81–124. doi:10.1007/s11214-010-9634-2.
- Ryder, G., and J. A. Wood (1977), Serenitatis and imbrrium impact melts—Implications for large-scale layering in the lunar crust, in *Lunar and Planetary Science Conference*.
- Salisbury, J. W. (1993), Mid-infrared spectroscopy: Laboratory data, in *Remote Geochemical Analysis: Elemental and Mineralogical Composition*, pp. 79–98, Cambridge Univ. Press, Cambridge, U. K.
- Salisbury, J. W. (1997), Thermal Infrared Spectra of Lunar Soils, *Icarus*, 130(1), 125–139. doi:10.1006/icar.1997.5809.
- Salisbury, J. W., G. R. Hunt, and L. M. Logan (1973), Infrared spectra of Apollo 16 fines, *Lunar and Planetary Science Conference*, 4, 3191.
- Shearer, C. K., and J. Papike (1999), Magmatic evolution of the Moon, *Am. Mineral.*, 84, 1469–1494.
- Shepard, M. K., R. A. Brackett, and R. E. Arvidson (1995), Self-affine (fractal) topography: Surface parameterization and radar scattering, *J. Geophys. Res.*, 100(E6), 11709–11.
- Smith, B. G. (1967), Lunar surface roughness: Shadowing and thermal emission, *J. Geophys. Res.*, 72(16), 4059–4067.
- Spencer, J. R. (1990), A rough-surface thermophysical model for airless planets, *Icarus*, 83(1), 27–38. doi:10.1016/0019-1035(90)90004-S.
- Taylor, L. A., C. M. Pieters, L. P. Keller, R. V. Morris, and D. S. McKay (2001), Lunar mare soils: Space weathering and the major effects of surface-correlated nanophase Fe, *J. Geophys. Res.*, 106(E11), 27985–27. doi:10.1029/2000JE001402.
- Taylor, S. R., M. D. Norman, and T. M. Esat (1993), The Mg-suite and the highland crust: An unsolved enigma, *Lunar and Planetary Science Conference*, vol. 24.
- Tompkins, S., and C. M. Pieters (1999), Mineralogy of the lunar crust: Results from Clementine, *Meteorit. Planet. Sci.*, 34(1), 25–41.
- Warner, J., C. Simonds, and W. Phinney (1976), Genetic distinction between anorthosites and Mg-rich plutonic rocks: new data from 76255, in *Lunar and Planetary Science Conference*, pp. 915–917.
- Warren, P. (1986), Anorthosite assimilation and the origin of the Mg/Fe-related bimodality of pristine Moon rocks: Support for the magmasphere hypothesis, *Lunar and Planetary Science Conference*, vol. 91.
- Wieczorek, M. A., and M. T. Zuber (2001), The composition and origin of the lunar crust: Constraints from central peaks and crustal thickness modeling, *Geophys. Res. Lett.*, 28(21), 4023. doi:10.1029/2001GL012918.
- Wieczorek, M. A. et al. (2006), The constitution and structure of the lunar interior, *Rev. Mineral. Geochem.*, 60(1), 221–364. doi:10.2138/rmg.2006.60.3.
- Yamamoto, S. et al. (2010), Possible mantle origin of olivine around lunar impact basins detected by SELENE, *Nat. Geosci.*, 3(8), 533–536. doi:10.1038/ngeo897.
- Zuber, M. T. et al. (2010), The Lunar Reconnaissance Orbiter laser ranging investigation, *Space Sci. Rev.*, 150(1–4), 63–80. doi:10.1007/s11214-009-9511-z.